UC Berkeley
UC Berkeley Previously Published Works

Title

Anode Catalysts in Anion-Exchange-Membrane Electrolysis without Supporting Electrolyte: Conductivity, Dynamics, and Ionomer Degradation

Permalink

https://escholarship.org/uc/item/7w20j8z6

Journal

Advanced Materials, 34(35)

ISSN

0935-9648

Authors

Krivina, Raina A
Lindquist, Grace A
Beaudoin, Sarah R
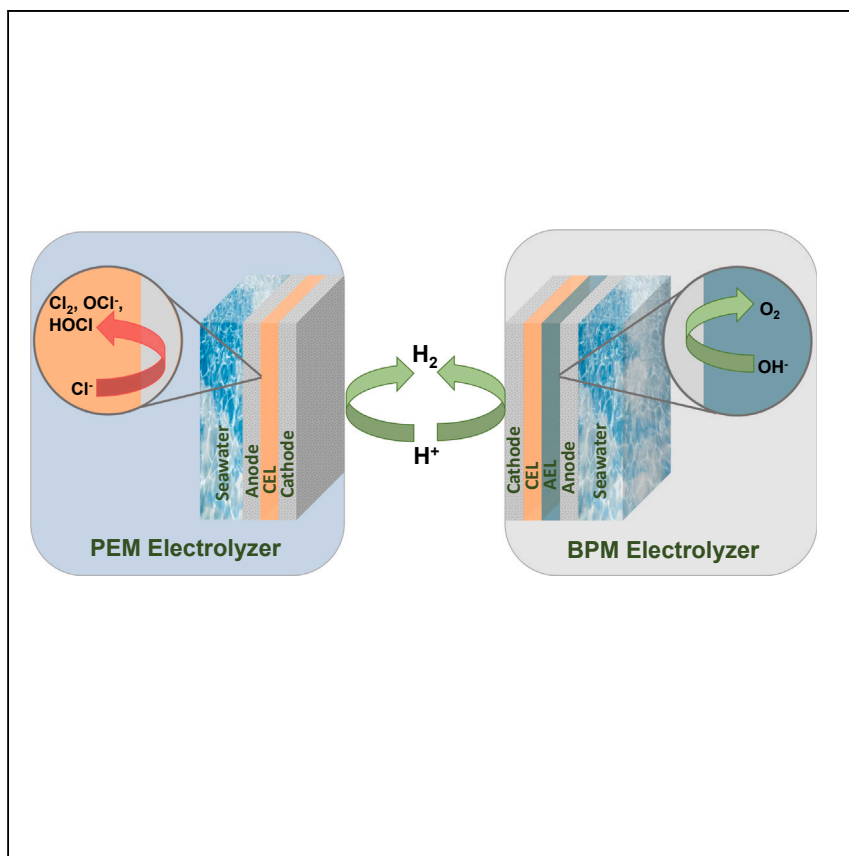et al.

Publication Date

2022-09-01

DOI

10.1002/adma.202203033

Peer reviewed

Article

Hydrogen production with seawater-resilient bipolar membrane electrolyzers

PEM Electrolyzer

BPM Electrolyzer

Daniela H. Marin, Joseph T. Perryman, McKenzie A. Hubert, ..., Shannon W. Boettcher, Adam C. Nielander, Thomas F. Jaramillo

swb@uoregon.edu (S.W.B.)
anieland@slac.stanford.edu (A.C.N.)
jaramillo@stanford.edu (T.F.J.)

Highlights

BPMWE devices promote direct electrolysis of seawater by limiting Cl^- oxidation

Impact of ion impurities on cell voltage was quantified for BPMWE and PEMWE devices

Failure modes have been explored for pure and impure water electrolysis conditions

Pathways forward are highlighted for improving BPM-based impure water electrolyzers

Our evaluation of bipolar membrane electrolyzers for seawater electrolysis highlights a step forward in addressing the water-energy nexus. Our discussions of device physics and ion-transport methods help translate basic science to sustainable energy systems—particularly those that require the prevention of deleterious side reactions that produce corrosive byproducts. This architecture is generalizable to water sources with various impurity compositions, aligning with the need for electrolyzers that enable the electrolysis of complex mixtures.

Article

Hydrogen production with seawater-resilient bipolar membrane electrolyzers

Daniela H. Marin,[1,2,5] Joseph T. Perryman,[1,2,5] McKenzie A. Hubert,[1,2] Grace A. Lindquist,[3] Lihaokun Chen,[3] Ashton M. Aleman,[1,2] Gaurav A. Kamat,[1,2] Valerie A. Niemann,[1,2] Michaela Burke Stevens,[2] Yagya N. Regmi,[4] Shannon W. Boettcher,[3,*] Adam C. Nielander,[2,*] and Thomas F. Jaramillo[1,2,6,*]

SUMMARY

Generation of H_2 and O_2 from untreated water sources represents a promising alternative to ultrapure water required in contemporary proton exchange membrane-based electrolysis. Bipolar membrane-based devices, often used in electrodialysis and CO_2 electrolysis, facilitate impure water electrolysis via the simultaneous mediation of ion transport and enforcement of advantageous microenvironments. Herein, we report their application in direct seawater electrolysis; we show that upon introduction of ionic species such as Na^+ and Cl^- from seawater, bipolar membrane electrolyzers limit the oxidation of Cl^- to corrosive OCl^- at the anode to a Faradaic efficiency (FE) of 0.005%, while proton exchange membrane electrolyzers under comparable operating conditions exhibit up to 10% FE to Cl^- oxidation. The effective mitigation of Cl^- oxidation by bipolar membrane electrolyzers underpins their ability to enable longer-term seawater electrolysis than proton exchange membrane assemblies by a factor of 140, suggesting a path to durable seawater electrolysis.

INTRODUCTION

The sustainable generation of chemical fuels such as H_2 offers a means to address the long-duration energy-storage challenge and to enable a next-generation, carbon-neutral chemical industry.[1] To this end, low-temperature water electrolysis driven by renewable electricity is a promising route to inexpensive, sustainably produced H_2 via the hydrogen evolution reaction (HER). While traditional membrane electrolyzers rely on ultrapure water feeds to generate H_2 and O_2, the direct electrolysis of impure water sources, e.g., seawater, could have inherent advantages, enabling broader access to water feedstocks while reducing capital costs by mitigating the need for on-site water purification.[2–6] However, electrolyzing seawater to generate H_2 and O_2 introduces distinct challenges in comparison to electrolyzing ultrapure water. One critical challenge arises from the high concentrations of ionic species (e.g., Cl^-, Na^+, SO_4^{2-}, Mg^{2+}, Ca^{2+}, etc.)—particularly Cl^-—in seawater. The Cl^- oxidation reaction (COR) generates corrosive "free chlorine" species (i.e., Cl_2, HOCl, OCl^-) at the electrolyzer anode. Although the electro-oxidation of Cl^- to Cl_2 (i.e., the chlorine evolution reaction [ClER]) is a critical industrial process (e.g., chlor-alkali process),[7] COR poses significant challenges to the safety, efficiency, and durability of seawater electrolyzers during operation.[8–12] Mitigating the COR with impure water feed also opens the possibility of making use of a pure O_2 stream from the anode for uses including undersea operations and life-support.

CONTEXT & SCALE

Direct seawater electrolysis offers a pathway toward low-cost H_2 and O_2 using abundant water feedstocks. However, high concentrations of ions present in seawater complicate electrolyzer operation. Cl^- ions, for example, can oxidize to corrosive and toxic byproducts. This presents a challenge to the safe and long-term operation of seawater electrolysis devices. In this work, we highlight fundamental principles of operation for a robust electrolysis system that leverages ion-selective membranes to control the transport and oxidation of Cl^- under both simulated and real seawater electrolysis conditions. We observe significantly improved bipolar membrane device lifetimes compared with those of proton-exchange membrane devices under real seawater conditions. This work motivates efforts to further develop impurity-tolerant electrolyzers and to advance seawater electrolysis systems that could enable green H_2 production and decarbonize critical sectors of the global economy.

The COR can, in principle, be suppressed by (1) decreasing anode catalyst selectivity for the COR, (2) modifying the anodic microenvironment to disfavor Cl⁻ oxidation, and/or (3) decreasing Cl⁻ access to the anode.[12–15] Developing catalysts that strongly favor the 4-electron oxygen evolution reaction (OER) over the 2-electron COR at relevant applied potentials is an active area of research.[16,17] IrO_x is an efficient precious-metal OER catalyst in Cl⁻-free electrolytes, but in electrolytes with Cl⁻ at concentrations as low as ∼30 mM it yields a high COR Faradaic efficiency (FE) of ∼86%.[18] Non-precious metal oxide catalysts, such as MnO_x, have shown promising OER selectivity (93%) in these same low-Cl⁻-concentration electrolytes, but material stability challenges in acidic pH are not yet resolved.[19,20] Strategies (2) and (3) are complementary and can be leveraged using device architectures to create local electrolyte conditions that disfavor COR, for example, by creating an alkaline anode environment where the oxidation of Cl⁻ is disfavored thermodynamically with respect to OER,[17,21] or by selectively inhibiting the transport of Cl⁻ to the anode, for example, using cation-selective membranes.

Here, we demonstrate how strategies (2) and (3) enabled near-complete suppression of Cl⁻ oxidation, even with a seawater feed. Our approach uses a bipolar membrane (BPM), composed of a cation exchange layer (CEL) combined with an anion exchange layer (AEL), integrated into a BPM water electrolyzer (BPMWE) device.[22–24] We found that an appropriately designed BPMWE, in concert with an asymmetric electrolyte feed in which seawater is only present at the cathode, mutually captured both the advantages of the CEL that limits Cl⁻ crossover to the anode (due to cation transport selectivity) and the AEL that provides a local alkaline anode pH (where OER catalysts have high selectivity and mitigate the COR), resulting in an inherently ion-tolerant seawater electrolyzer (Figure 1A). We evaluated the ion-transport properties, performance, selectivity, and durability of the BPMWEs with saline water feeds and compared them with monopolar proton exchange membrane water electrolyzers (PEMWEs). We demonstrated BPMWE devices operating with real seawater—collected from the Pacific Ocean (Half Moon Bay, CA, USA)—during sustained electrolysis to generate H_2 and O_2 at current densities of 250 mA cm⁻².

RESULTS AND DISCUSSION

BPMWE and PEMWE architectures were fabricated according to the designs in Figures 1 and S1. Extended descriptions of the experimental fabrication and electrochemical methods are provided in the experimental procedures section and in the supplemental information. Anion exchange membrane water electrolyzers (AEMWEs) were similarly fabricated, but significant Cl⁻ crossover precluded robust comparison to BPMWE and PEMWE (see Figure S2). The AEMWE is not examined in detail in this work owing to its inability to circumvent anion crossover and subsequently maintain favorable anode pH over time. It should be noted that, similar to the case of the BPMWE, Pourbaix analysis suggests that an AEMWE could be expected to operate without generating significant corrosive species and may also represent an alternative to the PEMWE architecture under conditions in which the AEMWE is durable to pH changes.

Electrolysis in deionized water and 0.5 M NaCl_aq

We characterized the j-V behavior of BPMWEs compared with PEMWEs under two different water feed conditions: a "symmetric" (same water feed composition fed to each electrode) deionized (DI)-water condition and an "asymmetric" (different feed composition fed to each electrode) saline condition. In the symmetric DI water condition, high-purity DI water (18.2 MΩ cm) was circulated through both the anode

[1]Department of Chemical Engineering, Stanford University, Stanford, CA 94305, USA

[2]SUNCAT Center for Interface Science and Catalysis, SLAC National Accelerator Laboratory, Menlo Park, CA 94025, USA

[3]The Department of Chemistry and Biochemistry and the Oregon Center for Electrochemistry, University of Oregon, Eugene, OR 97403, USA

[4]Manchester Fuel Cell Innovation Centre, Department of Natural Sciences, Manchester Metropolitan University, Manchester, UK

[5]These authors contributed equally

[6]Lead contact

*Correspondence: swb@uoregon.edu (S.W.B.), anieland@slac.stanford.edu (A.C.N.), jaramillo@stanford.edu (T.F.J.)
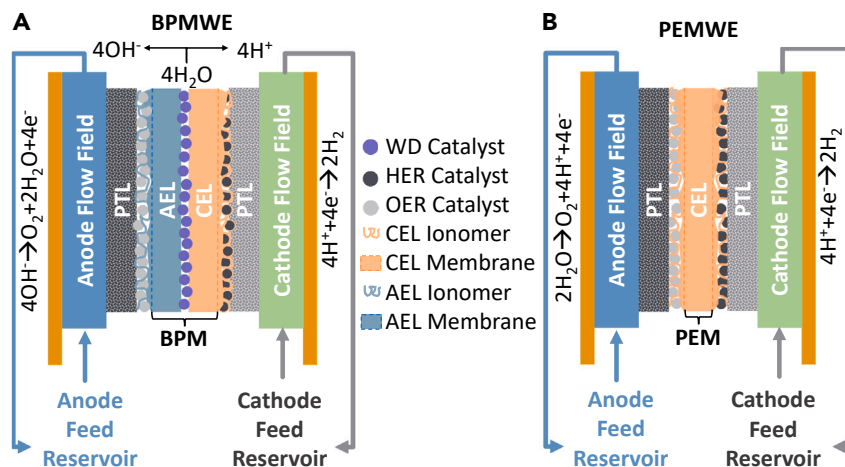
Figure 1. BPMWE and PEMWE device schematics

(A) Cross-sectional schematic of a zero-gap BPMWE and (B) cross-sectional schematic of a zero-gap PEMWE, illustrating the positioning of catalyst/ionomer-coated porous transport layers (PTL) relative to their respective ion-exchange membranes, as well as the circulation scheme that was used for all electrolyzer experiments. Reservoirs were heated to 60°C, resulting in a measured temperature of 50°C at the electrolyzer body (see supplemental information). Schematics are not drawn to scale. In these electrolyzers, CEL is defined as being the Nafion membrane as well as the Nafion ionomer of the catalyst layer(s), while AEL is defined as being the PiperION membrane and the PiperION ionomer of the catalyst layer.

and the cathode chambers (Figures 1A and 1B). In the asymmetric saline condition, we simulated seawater using 0.5 M NaCl$_{aq}$, approximating the ~0.55 M Cl$^-$ and ~0.47 M Na$^+$ concentrations in seawater.[25] The 0.5 M NaCl$_{aq}$ was fed to the cathode chamber while DI water was fed to the anode chamber. This asymmetric operating mode mimicked the conditions of an electrolyzer operating with seawater fed only to the cathode while facilitating measurements of ion crossover (Cl$^-$/Na$^+$) and Cl$^-$ oxidation behavior (see below).

Using symmetric DI water feeds, the voltage required to operate the PEMWE was 60 mV less than the BPMWE at j = 50 mA cm^{-2}, increasing to a voltage difference of 670 mV at j = 500 mA cm^{-2} (Figures 2A and 2B; Table 1). The voltage differences between the two devices is broadly consistent with recent reports on state-of-the-art performance for PEMWEs and BPMWEs.[26,27] The difference is attributed to the energy input required to drive water dissociation (WD, H$_2$O → H$^+$ + OH$^-$) at the CEL/AEL junction of the BPMWE, as well as the superior performance of a Nafion proton exchange ionomer in comparison to a PiperION-A40 anion exchange ionomer; AEL ionomers are more susceptible to oxidative degradation mechanisms than CEL ionomers has been highlighted in recent work.[10,25–28]

For both the PEMWE and BPMWE, using 0.5 M NaCl$_{aq}$ as the cathode feed (Figures 2A and 2B) increased total cell voltage with respect to the symmetric DI water-fed conditions (Table 1). We hypothesize that a significant fraction of the PEMWE/BPMWE performance loss reflects decreased [H$^+$] at the cathode-CEL interface due to the exchange between Na$^+$ and H$^+$ in the initially protonated CEL.[28] We interpret the transient voltage spikes seen in Figure 2C, which are only observed as the applied current density was changed in the presence of 0.5 M NaCl$_{aq}$, to be a result of a changing steady-state [Na$^+$] and [H$^+$] at the cathode-CEL interface; these concentration changes are likely due to shifts in the balance between diffusion and migration of both cations. As current density increases, H$^+$ migration toward the
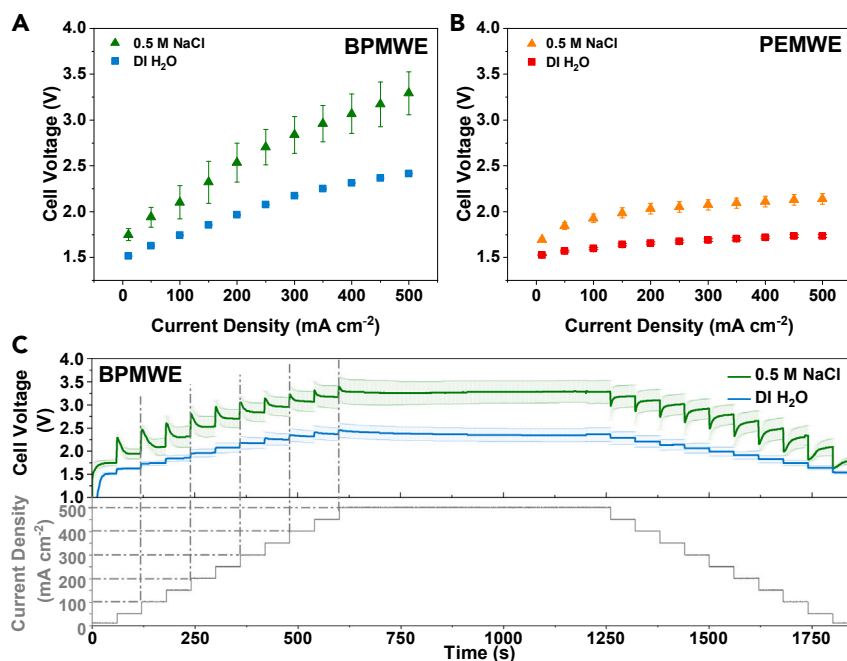
Figure 2. Characterization of device performance in deionized water and in 0.5 M NaCl
(A and B) Polarization curves with 0.5 M NaCl$_{aq}$ (green, orange triangles) as the cathode feed compared with DI H$_2$O (blue, red squares) as the cathode feed in a BPMWE (A) and a PEMWE (B). (C) Voltage versus time during stepped chronopotentiometry with (green) and without (blue) 0.5 M NaCl$_{aq}$ in a BPM electrolyzer cathode feed. On the lower y axis, the gray trace is the corresponding applied current density profile during stepped chronopotentiometry. Error bars in all cases represent a single standard deviation extracted from no less than three replicate experiments.

cathode-CEL interface increases relative to Na$^+$ diffusion into the same interface, leading to a decrease in voltage over time owing to a progressively more protonated CEL. The reverse is true when decreasing the current density, which results in a progressively less protonated, more sodiated cathode-CEL interface. Hence, a steady-state [H$^+$] at the cathode-CEL interface reflects a balance between multiple transport processes—including the diffusion of Na$^+$ from the bulk solution toward the cathode-CEL interface and migration of H$^+$ generated at the anode or WD layer toward the cathode (discussed below). The generation of local pH gradients over time between the anode and cathode in these systems may also contribute to observable changes in cell voltage owing to the decrease in reactant (i.e., H$^+$, OH$^-$) concentration—direct measurements of local pH at the electrode-electrolyte interface are the target of future work.

The BPMWE cell voltage was more affected by the addition of NaCl to the feed at 500 mA cm^{-2} than the PEMWE cell voltage (ΔV_{BPMWE} = 0.9 V; ΔV_{PEMWE} = 0.41 V). We assigned this difference to losses associated with WD and/or the AEL-anode

Table 1. Total cell voltages required to drive PEMWE and BPMWE devices at various applied current densities under DI water-fed conditions and asymmetric 0.5 M NaCl$_{aq}$ fed conditions

	DI water j = 50 mA cm^{-2}	DI water j = 500 mA cm^{-2}	0.5 M NaCl$_{aq}$ j = 50 mA cm^{-2}	0.5 M NaCl$_{aq}$ j = 500 mA cm^{-2}	ΔV_{cell} j = 500 mA cm^{-2} ($V_{NaCl} - V_{DI}$)
V_{cell} PEMWE (V)	1.57 ± 0.01	1.73 ± 0.02	1.84 ± 0.04	2.14 ± 0.06	0.41 ± 0.06
V_{cell} BPMWE (V)	1.63 ± 0.02	2.4 ± 0.2	1.94 ± 0.07	3.3 ± 0.2	0.9 ± 0.3

catalyst interface of the BPMWE, as the cathode catalyst environments are identical in both electrolyzers. Impedance analysis (Figures S3–S9, Note S4) suggests that the additional performance losses for the BPMWE can be attributed in part to increased WD resistance ($\Delta R_{WD,500\ mA}$ = 33 mΩ) in the BPMWE upon the addition of NaCl, along with higher series resistance ($\Delta R_{s,500\ mA}$ = 249 mΩ) compared with the PEMWE ($\Delta R_{s,\ 500\ mA}$ = 43 mΩ) (Figure S9). As anion exchange polymers generally demonstrate lower ionic conductivity due to the intrinsically lower mobility of OH^- relative to H^+ in cation exchange polymers,[29] we expect that conductivity losses from competing OH^-/Cl^- transport in the AEL will have a larger effect on performance relative to competing H^+/Na^+ transport in the CEL. Thus, we attribute the increased series resistance to a decrease in OH^- conductivity in the AEL as well as in the ionomer in the catalyst layer.[30] Cl^- or Na^+ ions that reach the BPM junction might also block WD catalyst active sites, contributing to the increase in R_{WD}. Careful selection of membranes, operating conditions, and catalyst identity are all potential routes to mitigating WD catalyst poisoning.

Ion crossover dynamics

To probe the ion-transport mechanisms that underpin PEMWE and BPMWE operation under saline conditions, we evaluated both electrolyzer architectures in the asymmetric saline electrolyte feed mode. Figures 3A and 3B depict the rate of Cl^- and Na^+ transport, respectively, from the cathode to anode chambers for both BPMWEs and PEMWEs with 0.5 M $NaCl_{aq}$ circulating at the cathode and DI water at the anode. In the absence of an applied current, there was no statistical difference in the rate of Na^+ and Cl^- crossover from cathode to anode, consistent with the electroneutrality requirements that Na^+ and Cl^- move through the membrane together.[31] Upon application of current, Na^+ transport is significantly suppressed, decreasing by ~3× in the PEMWE and ~13× in the BPMWE. The decreased Na^+ transport rate is consistent with the direction of the applied voltage driving positively charged species from the anode to the cathode. We ascribe the additional decrease in Na^+ crossover rate in the BPM to the AEL further blocking cation movement by Donnan exclusion (Figure 3C). Conversely, applied current did not have a significant influence on Cl^- transport (Figure 3A). The low crossover rate of Cl^- for both the BPMWE and PEMWE is consistent with a Donnan exclusion effect at the cathode/CEL interface (Figure 3C) that limits the crossover of negatively charged species despite a large concentration gradient in Cl^- between the cathode and anode feeds (~5 M_{Cl^-} mm^{-1}) favoring diffusive Cl^- crossover.[32] The similarity in Cl^- ion flux (J) across the BPMWE and PEMWE ($J^{Cl^-}_{avg,BPMWE}$ = 7.5 × 10^{-9} M cm^{-2} s^{-1} and $J^{Cl^-}_{avg,PEMWE}$ = 8.0 × 10^{-9} M cm^{-2} s^{-1}), regardless of current density (j) suggests that the AEL does not modulate anion crossover rates, though it may offer important advantages when a wider array of ions (e.g., K^+, Mg^{2+}, Ca^{2+}) are present (e.g., real seawater feed). Based on the low Cl^- transport rates observed, the percent of current carried by Cl^- crossover was low (~1%) at low applied current densities (e.g., j = 50 mA cm^{-2}), and decreased to <0.1% with increased applied current densities for both the BPMWE and PEMWE (see supplemental information, Note S2 and Figure S10).[33] Increasing the applied current density from j = 50 mA cm^{-2} to j = 500 mA cm^{-2} did not have a further inhibitory effect on the Na^+ crossover rate nor a clear promoting effect on the Cl^- crossover rate. This suggests there may be some mechanism(s) beyond transport via migration influencing ion crossover rates, such as current-dependent membrane-transport-selectivity effects (i.e., preferential acceleration of more mobile H^+ or OH^- transport rather than less mobile Na^+ or Cl^- transport or other concentrated electrolyte effects).[34]

The ion crossover data show that the BPMWE inhibits Na^+ crossover, while both the BPMWE and PEMWE inhibit Cl^- transport. Neither Na^+ nor Cl^- transport was
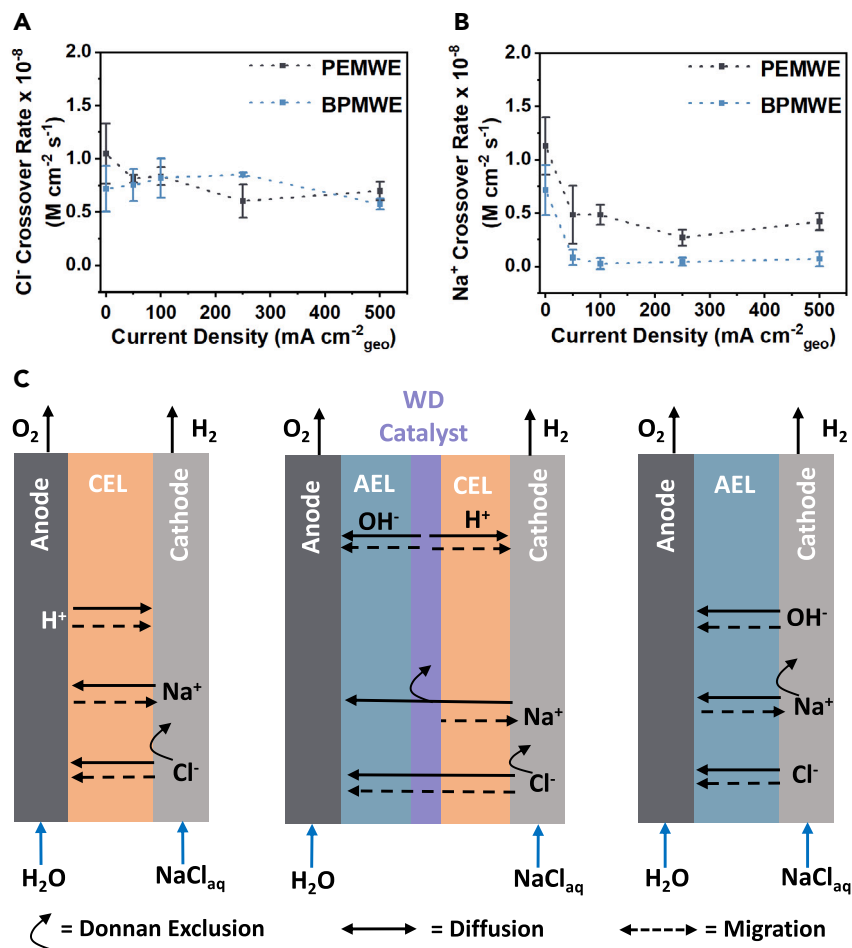
Figure 3. Ion-transport dynamics in membrane electrolyzers

(A and B) (A) Cl^- crossover rates versus applied current density, and (B) Na^+ crossover rates versus applied current density for BPMWE (blue) versus PEMWE (gray). ICP-MS was used to track the concentration of Na^+ and Cl^- and subsequently calculate ion crossover rates and fluxes. Error bars in all cases represent standard deviations from triplicated experimental data. These rates are described as molar fluxes defined with units of $M\ cm^{-2}\ s^{-1}$. We note that both cathode and anode chamber contained 1 L of solution, enabling the ready conversion of these units to $mol\ cm^{-2}\ s^{-1}$. Connecting lines are guides for data interpretation.

(C) Proposed key ion-transport effects for PEMWE (left), BPMWE (middle), and AEMWE (right), including diffusion (solid arrows), migration (dashed arrows), and Donnan exclusion effects (curved arrows) that dictate the transport of ions across the ion-exchange membranes.

significantly affected by increasing migration driving forces beyond j, suggesting that migration forces are not the sole driver of the observed ion-transport phenomenon. This discrepancy may highlight competition with vehicular and/or Grotthuss transport of H^+ and OH^- through the CEL and AEL, respectively.[35] In any case, however, the total charge carried via Cl^- migration is very low for both membrane architectures, capturing the advantage of the CEL in limiting Cl^- crossover and thereby inhibiting COR at the anode under asymmetric electrolyte conditions.

Cl^- electro-oxidation

Under asymmetric 0.5 M $NaCl_{aq}$ feed conditions, only Cl^- that crossed from cathode to anode should be available for oxidation to free chlorine species. Despite similar $J_{avg}Cl^-$ in the PEMWE and BPMWE, and thus expected similar $[Cl^-]$ in the anode
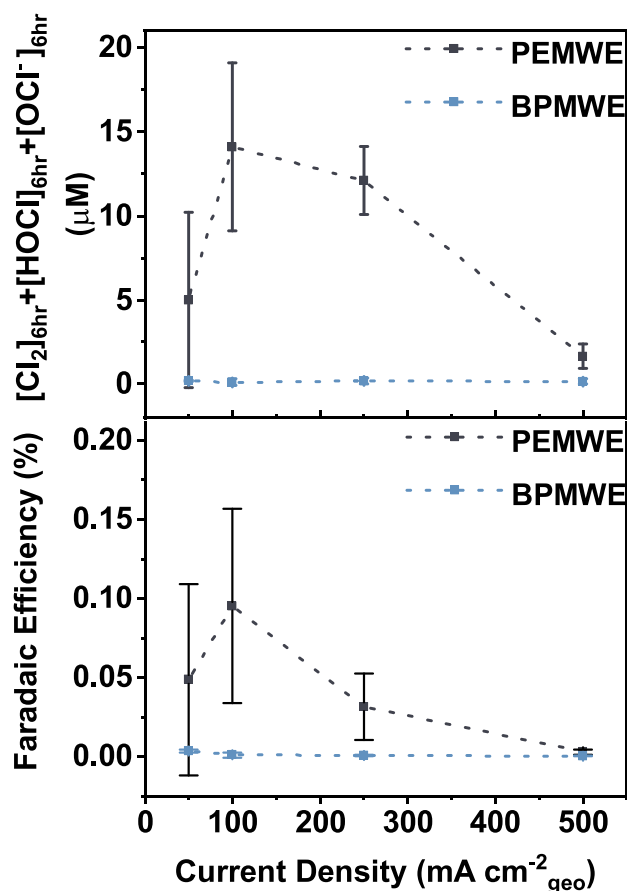
Figure 4. Chloride electro-oxidation behavior
BPMWE (blue) and PEMWE (gray) free chlorine concentrations after 6 h of 0.5 M NaCl$_{aq}$ electrolysis (top) and Faradaic efficiency for Cl$^-$ oxidation to free chlorine (bottom). Error bars are single standard deviations from triplicate experiments.

chamber, we observed a maximum FE = 0.095% for COR at j = 100 mA cm^{-2} in the PEMWE, significantly higher than the observed FE = 0.001% to COR for the BPMWE (Figure 4 and Note S1).

Corrosive free chlorine species are known to spontaneously degrade over time due to several factors: temperature, light, pH, and ionic strength of the solution.[36] We found the rate of free chlorine loss in both devices was nearly identical when present at equal initial concentrations (Figure S11). This excludes the possibility that differential free chlorine degradation rates explain the differences in COR FE between the two electrolyzer architectures. To further understand to the interesting trend in COR FE behavior observed for the PEMWE compared with the BPMWE shown in Figure 4, we also analyzed the COR in a three-electrode H-cell configuration with 0.5 M NaCl$_{aq}$ as the electrolyte at both j = 100 mA cm^{-2} and j = 250 mA cm^{-2}. We observed a COR FE of 4.0% at j = 100 mA cm^{-2} and 1.1% at j = 250 mA cm^{-2} in the acidic "simulated" H-cell PEMWE anode microenvironment, compared with <0.01% in the alkaline simulated BPMWE anode microenvironment (Figure S12) at both current densities. These data are in agreement with the trend that COR FE decreases at current densities beyond 100 mA cm^{-2} in the electrolyzer configuration and further indicate that the more acidic local pH of the PEMWE anode microenvironment promotes COR while the more basic pH present in the BPMWE anode
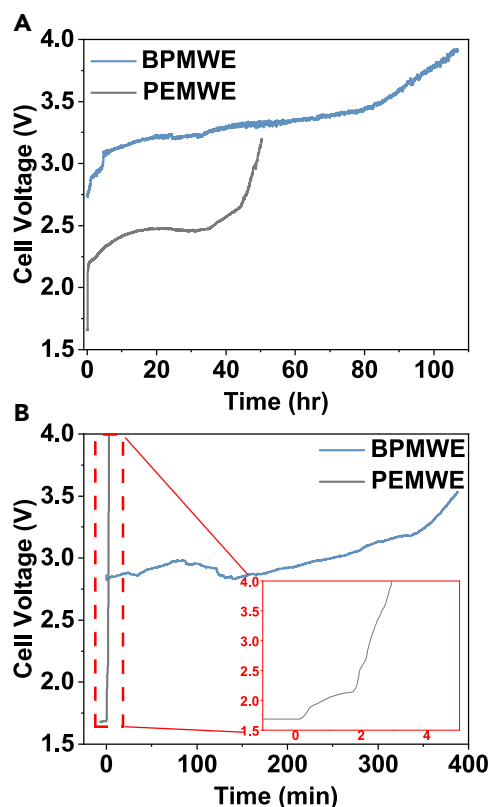
Figure 5. Device stability during real seawater electrolysis

V-t behavior for a BPMWE (blue) and a PEMWE (gray) at a fixed current of 250 mA cm^{-2} (A) with seawater as the cathode feed and DI water as the anode feed, and (B) with seawater fed to both cathode and anode. Inset highlights the entirety of the PEMWE experiment where immediate failure was observed. The first voltage increase at t = 0 min coincides with exchanging the cathode feed for seawater and the second voltage increase ~2 min coincides with exchanging the anode feed for seawater.

microenvironment suppresses the generation of corrosive free chlorine species. These observations are also consistent with more favorable thermodynamics at more alkaline pH for OER with respect to to COR (Figure S13).[21] We also found the simulated PEMWE anode FE for COR decreasing from 4.0% to 1.1% from 100 to 250 mA cm^{-2} to be consistent with the decreasing COR FE with increased current density observed in the electrolyzer configuration (Figures 4 and S12).

Electrolyzer stability with 0.5 M NaCl$_{aq}$ and seawater

Under galvanostatic conditions with asymmetric 0.5 M NaCl$_{aq}$ feed conditions, both the BPMWE and PEMWE demonstrated cell voltage degradation rates ($\Delta V_{6\,h}$) below 50 mV h^{-1} over the course of 6 h for a range of current densities. The BPMWE showed a smaller average voltage degradation rate than the PEMWE at all current densities except 500 mA cm^{-2} (Figure S14). However, the standard deviation in the measurements (Figure S15; Table S1) precluded our ability to determine with sufficient confidence that either electrolyzer voltage was more stable over 6 h of asymmetric 0.5 M NaCl electrolysis. Building on the promising results observed for electrolyzers operating under asymmetric saline feed conditions, we evaluated the performance of BPMWEs and PEMWEs operating with real seawater acquired from Half Moon Bay, CA. Figure 5A shows the observed cell voltage for both electrolyzer architectures operating at 250 mA cm^{-2} upon introduction of seawater to their

cathode feeds. Here, the increase in total cell voltage was 0.84 V in the BPMWE—slightly higher than the increase of 0.75 V with 0.5 M NaCl$_{aq}$. Similarly, the increase in seawater-fed cell voltage for the PEMWE was 0.82 V, compared with 0.41 V with 0.5 M NaCl$_{aq}$. These results highlight the additional voltage sensitivity for both electrolyzer architectures, but particularly for the PEMWE, to the presence of the other mono-, di-, and tri-valent ionic constituents present in real seawater.

For the first 6 h, the stability of a BPMWE with seawater as the cathode feed was within experimental error of a BPMWE fed with 0.5 M NaCl$_{aq}$ (Figures 5A and S15). The seawater-fed electrolysis experiments demonstrated $\Delta V_{6\,h}^{BPM}$ = 29 ± 20 mV h^{-1} over 6 h, as compared with 28 ± 8 mV h^{-1} for 0.5 M NaCl$_{aq}$ experiments (Figures S14 and S15) and ~15 mV h^{-1} for state-of-the-art BPMWEs operating in symmetric DI water-fed conditions.[27] In DI water, the voltage loss over time is attributed to anion exchange polymer degradation.[37,38] Analysis of the bulk cathode and anode feed pH changes over time in real seawater electrolysis experiments (Figure S16) reveal that performance losses may be correlated with increasing pH gradients across the device, giving rise to voltage losses.[39] After >100 h of continuous BPMWE operation at 250 mA cm^{-2}, free chlorine had only formed with an FE of 0.005% and is therefore not believed to contribute signficantly to the observed voltage degradation rate. Under the same asymmetric seawater conditions, the PEMWE failed after ~50 h and had rapidly generated more free chlorine (~20 μM) in the first 24 h of operation than the BPMWE had over the course of >100 h operation. This accelerated PEMWE voltage degradation is consistent with our observation that the formation of corrosive free chorine reduces device longevity (Figure S17). Although the BPMWE cell voltage was more sensitive than the PEMWE cell voltage to the inclusion of the 0.5 M NaCl in the cathode feed (Table 1), we believe that the extended electrolysis time of the asymmetric seawater experiments accentuated the difference in cell voltage stability engendered by differential production of free chlorine in the PEMWE versus the BPMWE.

When seawater was introduced to both the cathode feed and the anode feed, the increase in total cell voltage was 0.90 V for the BPMWE relative to symmetric DI water feed conditions. No voltage spike was quantified for the PEMWE upon addition of real seawater to its feeds because the voltage rapidly increased until failure within 3 min of operation (Figure 5B), likely due to the generation of corrosive free chlorine species at its acidic anode-CEL environment. After 3 min of electrolysis with seawater fed to both the anode and cathode, COR FE was 10% for the PEMWE, while the BPMWE did not generate any detectable free chlorine species throughout 7 h of direct, unprocessed seawater electrolysis. Post-experiment analysis (Figures S18–S22) suggests the precipitation of divalent cation hydroxides—predominately of Mg(OH)$_2$—as an additional contributor to performance loss in real seawater for both architectures, as has been discussed in previous work.[15] Additional post-experiment ICP-MS analysis is presented in Tables S2 and S3, illustrating relatively low levels of Ir and Pt loss from the anode of each electrolyzer.

Conclusions

We designed, fabricated, and evaluated PEMWEs and BPMWEs operating under asymmetric and symmetric saline electrolyte conditions to generate H$_2$ and O$_2$ at high current densities for extended periods of time. We quantified the effect of feed contamination on performance in terms of energy efficiency and device durability, charting a new path and design principles for deployable, durable, and efficient direct electrolysis of impure water.

Despite higher operating voltages than PEMWEs, BPMWEs provided the combined advantages of mitigating undesired ion transport (e.g., Cl^- crossover in this case) and controlling selectivity for O_2 production in high-salinity testing conditions. We propose that Na^+ transport in/through the protonated Nafion ionomer of both electrolyzers, however, likely reduces the H^+ concentration at the cathode, slowing HER kinetics and illustrating the need for microenvironment design at the electrode interfaces. Interestingly, the flux of both Na^+ and Cl^- across the BPM were largely independent of cell voltage and (total) current density. This suggests more complex interactions beyond standard dilute electrolyte theory and motivates additional work to improve the understanding of operative transport dynamics in impure water electrolyzers and other electrochemical technologies. The BPMWE also provides a locally basic pH at the anode and thus inhibits the generation of corrosive free chlorine that is formed in the acidic PEMWE anode and leads to rapid PEMWE failure in seawater.

The robust zero-gap BPM seawater electrolyzer reported here operated at current densities of 250 mA cm^{-2} and serves as a benchmark for membrane electrolyzer durability with impure feeds, providing a unique route to avoid Cl^- oxidation, increase efficiency, and prevent device failure without requiring ultrapure water. Despite significant improvements in durability for the BPMWE compared with the PEMWE, decreased voltage stability for both systems fed with seawater indicates that other failure mechanisms arise from the more complex electrolyte composition. As such, deployment of these devices still requires significant improvements in cell voltage and durability; >50,000 h lifetimes and cell voltage degradation rates between 10 and 20 μV h^{-1} are common in commercial (pure water) electrolyzers.[40–43] To this end, device components such as membranes, porous transport layers (PTLs), flow-fields, and catalysts all remain viable targets for improving performance and durability for seawater electrolysis.[10,44]

EXPERIMENTAL PROCEDURES

Resource availability

Lead contact
Further information and requests for resources should be directed to and will be fulfilled by the lead contact, Thomas F. Jaramillo, at jaramillo@stanford.edu.

Materials availability
This study did not generate new unique reagents.

Data and code availability
The data generated during this study are available upon request to jaramillo@stanford.edu.

Materials
Electrodes and membranes were prepared according to recent reports.[27] NaCl (99.0% trace metals basis) was used as purchased from Sigma Aldrich in all saline water (0.5 M NaCl$_{aq}$) experiments. Cationic impurities of NaCl include Ca^{2+} (<0.002%), Mg^{2+} (<0.001%), K^+ (<0.005%) and $Fe^{2+/3+}$ (<2 ppm). Here, DI water refers to ultrapure DI water with a measured resistivity of approximately 18.2 MΩ cm. Nafion 212 and PiperION-A40 membranes and ionomers were used as the cation- and anion-selective layers (CEL and AEL), respectively, in the BPMWE. The BPMWE anode consisted of IrO_x nanoparticles (5–10 nm dia.) on a stainless-steel PTL while the PEMWE integrated the same IrO_x nanoparticles onto a platinized titanium PTL.

The cathode in both electrolyzers was Pt black (34 m^2 g^{-1}) deposited on Toray carbon paper PTL.

Anode preparation

Anodes for BPMWE and PEMWE devices were fabricated by preparing a catalyst ink and then spraying the ink onto a PTL substrate. To produce the ink, iridium oxide (0.1 g) (Fuel Cell Store), ultrapure DI water (0.5 g, 18.2 MΩ cm), isopropyl alcohol (1.7 g), and 5 wt% ionomer (BPMWE: PiperION [0.1 g] [Versogen]; PEMWE: Nafion 212 [0.1 g] [Sigma Aldrich]) were, in that order, added to a 20 mL glass scintillation vial. The vial was bath sonicated for 10–20 min or until the ink mixture was evenly dispersed. A 5 cm × 5 cm PTL substrate (BPMWE: stainless steel, 25AL3 [Bekaert Bekipor]; PEMWE: platinized titanium fiber felt, [Fuel Cell Store]) was prepared and the back of the layer was pencil traced with gridlines of a 4 cm × 4 cm square and weighed. The front of the PTL was framed with tape to make a 4 cm × 4 cm spray area and then placed onto a hotplate (100°C). Using a hand-held airbrush (Testors), the catalyst ink was sprayed perpendicular to the hotplate in a pulsed serpentine pattern (8–12 psi) until the catalyst reached the desired loading (2.5 mg cm^{-2}| 40 mg total). The surface was allowed to evaporate before spraying a new layer of catalyst by waiting about 5 s between each serpentine pattern. To weigh the catalyst mass between sprays, the tape frame was removed, and the electrodes were allowed to cool to room temperature before weighing. A new tape frame was placed around the active spray area. After the catalyst was sprayed, dilute ionomer solution (BPMWE: 2% PiperION; PEMWE: 5% Nafion) solution in ethanol was sprayed over the catalyst layer in a pulsed serpentine pattern until the ionomer overlayer reached 10%–20% of the catalyst mass weight (4–8 mg). The anodes were stored in a polystyrene container at room temperature until use.

Cathode preparation

Cathodes for the PEMWE and BPMWE were fabricated identically by preparing a catalyst ink and subsequently spraying the ink onto a carbon-based PTL. In detail, platinum catalyst (0.1 g) (Fuel Cell Store), ultrapure DI water (1.5 g, 18.2 MΩ cm), isopropyl alcohol (1.7 g), and 5 wt% Nafion (0.1 g), in that order, were added to a 20 mL glass scintillation vial. The vial was bath sonicated for 20–30 min or until the ink mixture was evenly dispersed. If the ink was not fully dispersed, the bath sonication was followed with 20 s of probe sonication pulses with 5 s rest for 1.5 min. A 5 cm × 5 cm Toray carbon PTL was cut, and the back of the layer was pencil traced with gridlines of a 4 cm × 4 cm square and weighed. The front of the PTL was framed with tape to make a 4 cm × 4 cm spray area and then placed onto a hotplate (100°C). Using a hand-held airbrush (Testors), the catalyst ink was sprayed perpendicular to the hotplate in a pulsed serpentine pattern (8–12 psi) until the catalyst reached the desired loading (2 mg cm^{-2}|32 mg total). The surface was allowed to evaporate before spraying a new layer of catalyst by waiting about 5 s between each serpentine pattern. To weigh the catalyst mass between sprays, the tape frame was removed, and the electrodes were allowed to cool to room temperature before weighing. A new tape frame was placed around the active spray area. After the catalyst was sprayed, a 5% Nafion solution was sprayed over the catalyst layer in a pulsed serpentine pattern until the ionomer overlayer reached 10%–20% of the catalyst mass weight (3.2–6.4 mg). The cathodes were stored in a polystyrene container at room temperature until use.

Bipolar membrane preparation

BPMs were prepared using a Nafion 212 (50.8 μm) (Fuel Cell Store) proton exchange membrane and ionomer as the CEL, PiperION TP-85 (40 μm) (Versogen) anion

exchange membrane and ionomer as the AEL, and a TiO_2 nanoparticulate WD catalyst layer. TiO_2 nanoparticles (0.1 g) (Nippon Aerosil) were dispersed in water (4.9 g). The ink was sonicated for 5 min. A small amount of this concentrated TiO_2-water "mother ink" (30 mg) was diluted in a water and IPA (2-propanol) mixture (0.47 g water, 1.7 g IPA). The diluted ink was bath sonicated for 5 min prior to spraying. The as-received Nafion membrane was removed from the plastic backing and soaked in DI water over night. The edges of the Nafion membrane (cut with scissors to 1.5 cm × 1.5 cm) was carefully taped onto a glass Petri dish ensuring no air bubbles were present, leaving a 1.2 cm × 1.2 cm area exposed, and the Petri dish was laid flat on a hot plate (90°C) in a fume hood. The diluted TiO_2 ink was then hand-sprayed ([Testors], perpendicular to the hot plate surface, 10 psi) onto the Nafion membrane in bursts (~1 s). The burst pattern involved spraying 10 times, then rotating the sample 90° and repeating until the ink was completely used. The air flow from the fume hood and spray methodology were important in reproducing the TiO_2 loading and morphology on the Nafion membrane. When the entirety of the dilute TiO_2 ink was sprayed, the tape was carefully removed from the edges of the membrane, using water to help lift the tape. The edge of the membrane was marked to identify what side had been sprayed, and the membrane was stored in DI water until ready to assemble the electrolyzer, at which point it was combined with the PiperION anion exchange membrane.

Seawater treatment

Seawater was collected from Half Moon Bay, CA and filtered to remove suspended solids prior to incorporation into either electrolyzer reservoir during testing. This simple filtration mitigated potential clogging of the water feed diaphragm pumps (KNF Neuberger) by particulate matter during long-term circulation of the seawater.

Electrolyzer assembly

Commercial electrolyzer hardware (5 cm^2, [Fuel Cell Technologies]) was used in all tests, in configurations shown in Figure 1. A Ti flow field was used for the anode side, and a graphite flow field was used for the cathode side. Assembling from the anode side, gaskets (polyethylene terephthalate [PETE], 0.047″ for BPMWE, 0.037″ for PEMWE, cut with a 1 cm × 1 cm opening) were stacked on top of the titanium flow field. A porous Ti support was placed in the gasket opening followed by the anode PTL, catalyst side up. The PiperION membrane (1.5 × 1.5 cm) was placed on top of the PTL. The TiO_2-coated Nafion membrane was placed on top of the PiperION membrane, with the TiO_2 side facing down (toward the PiperION). Additional gaskets were placed on top (PETE, 0.037″ cut with a 1 cm × 1 cm opening) and the cathode PTL was placed in the gaskets, catalyst side down (facing the Nafion membrane). A Ti support was placed on top of the cathode PTL. The cathode flow field, current collector, and back plate were placed on top. The hardware was tightened to 50 lbs-in (5.65 N m) using a star pattern of tightening to ensure even compresion.

Electrolyte flow conditions

The electrolyzer was connected to two separate water re-circulating loops—one for the cathode and one for the anode. Each loop circulated to and from their own respective 1 L reservoirs of water heated to 60°C. The water was supplied to both the anode and cathode with a calibrated flow of 60 mL/min using diaphragm pumps (KNF Neuberger). Electrochemical measurements began when the cell temperature, as measured by a K-type thermocouple at the cathode back plate, reached 50°C (± 1°C), which took ~30 min for each experiment. The cell temperature was maintained at 50°C (±1°C) by tuning the water temperature in the reservoirs as appropriate.

Electrolyzer break-in and operation

A break-in procedure was performed before each experiment, with DI water circulating to both cathode and anode electrolyzer compartments. First, current was held at 10 mA for 1 min. The current was then sequentially stepped up in 50 mA increments from 50 to 500 mA, holding each current for 1 min prior to stepping to the next. In the final increment, current was held at 500 mA for a total of 10 min, at which point a "break-in potential" was recorded to ensure that baseline device performance was as expected. If the break-in voltage of a BPM was >2.5 V or of a PEM was >1.9 V at 500 mA cm^{-2}, the electrolyzer was disassembled and reassembled with a new membrane electrode assembly (MEA). This first sequence is coined as "CP1" and can be seen for all three membrane architectures in Figures S2A and S2B. Following this increasing first sequence of stepped chronopotentiometry, the current was stepped back down in 50 mA increments from 500 to 50 mA, again holding each current for 1 min, followed by 1 min at 10 mA. This decreasing sequence of stepped chronopotentiometry is coined as "CP2." Next, a rapid, increasing stepped chronopotentiometry sequence was performed starting at 10 mA for 10 s, and then again stepping the current in 50 mA increments from 50 to 500 mA holding each for 10 s. This last sequence is coined as "CP3." Polarization curves shown in Figures 2A and 2B were extracted from stabilized voltages at the end of each current step in CP1, prior to increasing applied current density. This method avoids spurious results that might otherwise arise from extracting voltages at non-steady-state membrane conditions.

Following the completion of CP3, a series of galvanostatic electrochemical impedance spectroscopy (GEIS) scans were performed at fixed current densities of 500 mA cm^{-2} (GEIS 4), 250 mA cm^{-2} (GEIS 5), 100 mA cm^{-2} (GEIS 6), 50 mA cm^{-2} (GEIS 7), and then at the target current density for long-term electrolysis (GEIS 8), with superimposed alternating currents (AC) having magnitudes of 10% of each respective direct current (DC). AC oscillation frequencies were scanned from 200 kHz to 20 mHz to extract circuit resistances, voltage-dependent charge-transfer resistances, and voltage-dependent water-dissociation resistances (in the case of a BPM) prior to the addition of simulated (0.5 M NaCl$_{aq}$) or real seawater.

After the break-in procedure, the current was held constant at either 0, 50, 100, 250, or 500 mA for 6 h. When the voltage reached a steady-state value (~5 min), either NaCl (29.22 g) was added to the cathode reservoir (1 L) to create a 0.5 M NaCl$_{aq}$ cathode feed solution, or pre-heated seawater from Half Moon Bay, CA was exchanged as the cathode feed solution, depending on the desired experiment. An aliquot of 5 mL was taken for inductively coupled plasma mass-spectrometry (ICP-MS) analysis (ThermoScientific iCAP RQ) and pH measurements (accumet BASIC, accuTupH probe) from the anode feed at t = 0 s (immediately before the salt was added), 1, 3, and 6 h. Aliquots of 10 mL were also taken from the anode feed for additional analysis via UV-vis to quantify free chlorine concentrations at elapsed times of 1, 3 and 6 h after the addition of NaCl. Throughout this constant current experiment, additional GEIS experiments were performed at the same current density (GEIS 10–16) to monitor changing impedance over time.

Inductively coupled plasma mass-spectrometry measurements

Trace element analysis (Tables S2 and S3) was performed with ICP-MS (ThermoFisher Scientific, iCAP RQ) using a parallel flow nebulizer (Burgener PEEK Mira Mist) and a Peltier-cooled Scott-type double-pass cyclonic spray chamber cooled to 2.7°C. Forward radio frequency plasma generator power was set to 1,550 W with argon flows of 14 L min^{-1} for carrier gas, 0.8 L min^{-1} for cooling gas, and 1.2 L min^{-1} for nebulizer gas. Sample and skimmer cones of nickel were

installed with a 4.5 mm robust insert to increase matrix tolerance for seawater. The ICP-MS was operated in helium kinetic energy discrimination (He KED) mode with a Qcell collision/reaction gas flowrate of 5 mL min^{-1}. Na and Cl standard solutions were prepared for a concentration range from 0.1 to 5 ppm using serial dilution of a NaCl standard (Ricca Chemical). Pt (Sigma Aldrich), Ir (Ricca Chemical), and Fe (Sigma Aldrich) standard solutions were prepared for a concentration range from 0 to 100 ppb using serial dilution. All measurements were performed with three repetitions of ten sweeps using a 100 ms dwell time and reported error bars correspond to the relative standard deviation (on average, ~5% RSD).

Three-electrode measurements

The three-electrode measurements (Figure S12) designed to evaluate Cl$^-$ electro-oxidation were executed using the appropriate PTL with catalyst and ionomer overlayer (e.g., stainless steel with IrO$_x$ and PiperION to simulate a BPMWE anode; Pt/Ti with IrO$_x$ and Nafion to simulate a PEMWE anode) as a working electrode in aqueous 0.5 M H$_2$SO$_4$ or 1 M NaOH with 0.5 M NaCl electrolytes to mimic the interface pH environment of PEMWE or BPMWE, respectively. Counter electrodes in all cases were the same catalyst and ionomer-coated carbon paper electrodes as were also used in the electrolyzer configuration and were separated from the working electrode by a Nafion membrane. Ag/AgCl reference electrodes were placed in the working electrode compartment of the Teflon H-cell to monitor working and counter electrode potentials. Electrolysis was performed both at a range of constant potentials near the onset of COR as well as at two current densities of relevance to this work (i.e., 100 and 250 mA cm^{-2}).

Chloride oxidation quantification

Cl$^-$ oxidation to free chlorine was quantified using a commercially available colorimetric N-diethyl-p-phenylenediamine (DPD) test (Thermo Scientific Orion Chlorine Free-DPD Powder Packs). Briefly, the contents of one as-received "DPD Powder Pack" were added to a 10 mL analyte solution in a 20 mL scintillation vial. The vial was shaken vigorously for 10 s. A vibrant pink color would develop if free chlorine was present in the aliquot. Immediately after adding DPD, the sample was placed into a disposable polystyrene UV-vis cuvette with a path length of 1 cm. The UV-vis spectrometer (Agilent Cary 6000i) was configured in double beam mode with DI water in the reference cuvette and scanned at 10 nm/s from 800 to 200 nm. Background scans were acquired by adding a DPD packet to DI water. To quantify free chlorine concentrations, absorbance was recorded at 552 nm. 552 nm is the wavelength of maximum absorbance of DPD when it has been oxidized by any free chlorine species to generate its "Wurster Dye" radical analog.[45,46] This absorbance was then converted to a free chlorine concentration according to an established calibration curve (Figure S23). To account for potential free chlorine degradation with time, we measured the rate of free chlorine concentration decrease in solutions that were flowed through BPMWE and PEMWE devices under (1) open circuit conditions, (2) electrolysis conditions at 500 mA cm^{-2}, and (3) two different anode PTL compositions (Figure S11). The rate of degradation in all cases was sufficiently slow on the timescale of our experiments as to be considered negligible.

X-ray photoelectron spectroscopy

Electrode surface composition was analyzed with a Phi VersaProbe 3 with monochromatized Al (Kα) radiation, 200 μm spot size, 50 W power, and 15 kV gun voltage. Samples were neutralized during acquisition with an electron flood gun and an Ar ion gun and spectral signatures were identified according to their binding energies relative to adventitious carbon signal at 284.8 eV.

Scanning electron microscopy

Electrode morphology was observed with a Thermo Fisher Scientific Apreo S LoVac Scanning Electron Microscope with Trinity detector system and NiCol electron column under high-vacuum conditions with an accelerating voltage of 15 kV (~1.0 nm beam resolution), a 10 pA beam current and a working distance of 10 mm. Scale bars were generated from pixel-calibrated image files in ImageJ software.

SUPPLEMENTAL INFORMATION

Supplemental information can be found online at https://doi.org/10.1016/j.joule.2023.03.005.

AUTHOR CONTRIBUTIONS

Conceptualization, D.H.M., J.T.P., M.A.H., G.A.L., L.C., M.B.S., A.C.N., S.W.B., and T.F.J.; methodology, D.H.M., J.T.P., M.A.H., A.M.A., G.A.K., V.A.N., Y.N.R., and A.C.N.; investigation, D.H.M., J.T.P., M.A.H., A.M.A., G.A.K., V.A.N., and A.C.N.; visualization, D.H.M. and J.T.P.; funding acquisition, S.W.B., T.F.J., M.A.H., and A.C.N.; project administration, S.W.B., A.C.N., and T.F.J.; supervision, S.W.B., T.F.J., and A.C.N.; writing – original draft, D.H.M. and J.T.P.; writing – review & editing, D.H.M., J.T.P., M.A.H., G.A.L., L.C., G.A.K., M.B.S., Y.N.R., S.W.B., A.C.N., and T.F.J.

DECLARATION OF INTERESTS

The authors have patents submitted and issued (US patent # 11,268,200) related to the content of this manuscript.

INCLUSION AND DIVERSITY

One or more of the authors of this paper self-identifies as an underrepresented ethnic minority in their field of research or within their geographical location. One or more of the authors of this paper self-identifies as a gender minority in their

REFERENCES

1. Gao, F.-Y., Yu, P.-C., and Gao, M.-R. (2022). Seawater electrolysis technologies for green hydrogen production: challenges and opportunities. Curr. Opin. Chem. Eng. 36, 100827. https://doi.org/10.1016/j.coche.2022.100827.

2. Caldera, U., and Breyer, C. (2017). Learning curve for seawater reverse osmosis desalination plants: capital cost trend of the past, present, and future. Water Resour. Res. 53, 10523–10538. https://doi.org/10.1002/2017WR021402.

3. Farràs, P., Strasser, P., and Cowan, A.J. (2021). Water electrolysis: direct from the sea. or not to be? Joule 5, 1921–1923. https://doi.org/10.1016/j.joule.2021.07.014.

4. Gao, L., Yoshikawa, S., Iseri, Y., Fujimori, S., and Kanae, S. (2017). An economic assessment of the global potential for seawater desalination to 2050. Water 9, 763. https://doi.org/10.3390/w9100763.

5. Wang, S., Liu, H., Gu, J., Sun, H., Zhang, M., and Liu, Y. (2019). Technology feasibility and economic viability of an innovative integrated ceramic membrane bioreactor and reverse osmosis process for producing UltraPure water from municipal wastewater. Chem. Eng. J. 375, 122078. https://doi.org/10.1016/j.cej.2019.122078.

6. Azinheira, G., Segurado, R., and Costa, M. (2019). Is renewable energy-powered desalination a viable solution for water stressed regions? A case study in Algarve, Portugal. Energies 12, 4651. https://doi.org/10.3390/en12244651.

7. O'Brien, T., Bommaraju, T.V., and Hine, F. (2005). Handbook of Chlor-Alkali Technology (Springer).

8. Kirk, D., and Ledas, A. (1982). Precipitate formation during sea water electrolysis. Int. J. Hydrog. Energy 7, 925–932. https://doi.org/10.1016/0360-3199(82)90160-4.

9. Dresp, S., Dionigi, F., Klingenhof, M., and Strasser, P. (2019). Direct electrolytic splitting of seawater: opportunities and challenges. ACS Energy Lett. 4, 933–942. https://doi.org/10.1021/acsenergylett.9b00220.

10. Lindquist, G.A., Xu, Q., Oener, S.Z., and Boettcher, S.W. (2020). Membrane electrolyzers for impure-water splitting. Joule 4, 2549–2561. https://doi.org/10.1016/j.joule.2020.09.020.

11. Millet, P., Ranjbari, A., de Guglielmo, F., Grigoriev, S.A., and Auprêtre, F. (2012). Cell failure mechanisms in PEM water electrolyzers. Int. J. Hydrog. Energy 37, 17478–17487. https://doi.org/10.1016/j.ijhydene.2012.06.017.

12. Dresp, S., Ngo Thanh, T., Klingenhof, M., Brückner, S., Hauke, P., and Strasser, P. (2020). Efficient direct seawater electrolysers using selective alkaline NiFe-LDH as OER catalyst in asymmetric electrolyte feeds. Energy Environ. Sci. 13, 1725–1729. https://doi.org/10.1039/D0EE01125H.

13. Veroneau, S.S., and Nocera, D.G. (2021). Continuous electrochemical water splitting from natural water sources via forward osmosis. Proc. Natl. Acad. Sci. USA 118. e2024855118. https://doi.org/10.1073/pnas.2024855118.

14. Han, J.-H., Jwa, E., Lee, H., Kim, E.J., Nam, J.-Y., Hwang, K.S., Jeong, N., Choi, J., Kim, H., Jeung, Y.-C., and Chung, T.D. (2022). Direct seawater electrolysis via synergistic acidification by inorganic precipitation and proton flux from bipolar membrane. Chem. Eng. J. 429, 132383. https://doi.org/10.1016/j.cej.2021.132383.

15. Han, J.H. (2022). Exploring the interface of porous cathode/bipolar membrane for mitigation of inorganic precipitates in direct seawater electrolysis. ChemSusChem 15, e202200372. https://doi.org/10.1002/cssc.202200372.

16. Consonni, V., Trasatti, S., Pollak, F., and O'Grady, W.E. (1987). Mechanism of chlorine evolution on oxide anodes study of pH effects. J. Electroanal. Chem. 228, 393–406. https://doi.org/10.1016/0022-0728(87)80119-5.

17. Dionigi, F., Reier, T., Pawolek, Z., Gliech, M., and Strasser, P. (2016). Design criteria, operating conditions, and nickel–iron hydroxide catalyst materials for selective seawater electrolysis. ChemSusChem 9, 962–972. https://doi.org/10.1002/cssc.201501581.

18. Vos, J.G., Liu, Z., Speck, F.D., Perini, N., Fu, W., Cherevko, S., and Koper, M.T.M. (2019). Selectivity trends between oxygen evolution and chlorine evolution on iridium-based double perovskites in acidic media. ACS Catal. 9, 8561–8574. https://doi.org/10.1021/acscatal.9b01159.

19. McCrory, C.C.L., Jung, S., Peters, J.C., and Jaramillo, T.F. (2013). Benchmarking heterogeneous electrocatalysts for the oxygen evolution reaction. J. Am. Chem. Soc. 135, 16977–16987. https://doi.org/10.1021/ja407115p.

20. Vos, J.G., Wezendonk, T.A., Jeremiasse, A.W., and Koper, M.T.M. (2018). MnOx/IrOx as selective oxygen evolution electrocatalyst in acidic chloride solution. J. Am. Chem. Soc. 140, 10270–10281. https://doi.org/10.1021/jacs.8b05382.

21. Pourbaix, M. (1974). Atlas of Electrochemical Equilibria in Aqueous Solution (National Association of Corrosion Engineers).

22. Berlinger, S.A., McCloskey, B.D., and Weber, A.Z. (2018). Inherent acidity of perfluorosulfonic acid ionomer dispersions and implications for ink aggregation. J. Phys. Chem. B 122, 7790–7796. https://doi.org/10.1021/acs.jpcb.8b06493.

23. Wang, J., Zhao, Y., Setzler, B.P., Rojas-Carbonell, S., Ben Yehuda, C., Amel, A., Page, M., Wang, L., Hu, K., Shi, L., et al. (2019). Poly(aryl piperidinium) membranes and ionomers for hydroxide exchange membrane fuel cells. Nat. Energy 4, 392–398. https://doi.org/10.1038/s41560-019-0372-8.

24. Vermaas, D.A., and Smith, W.A. (2016). Synergistic electrochemical CO_2 reduction and water oxidation with a bipolar membrane. ACS Energy Lett. 1, 1143–1148. https://doi.org/10.1021/acsenergylett.6b00557.

25. Dickson, A.G., and Goyet, C. (1994). Handbook of Methods for the Analysis of the Various Parameters of the Carbon Dioxide System in Sea Water. Version 2 (Oak Ridge National Lab).

26. Oener, S.Z., Foster, M.J., and Boettcher, S.W. (2020). Accelerating water dissociation in bipolar membranes and for electrocatalysis. Science 369, 1099–1103. https://doi.org/10.1126/science.aaz1487.

27. Chen, L., Xu, Q., Oener, S.Z., Fabrizio, K., and Boettcher, S.W. (2022). Design principles for water dissociation catalysts in high-performance bipolar membranes. Nat. Commun. 13, 3846. https://doi.org/10.1038/s41467-022-31429-7.

28. Pintauro, P.N., and Bennion, D.N. (1984). Mass transport of electrolytes in membranes. 2. Determination of sodium chloride equilibrium and transport parameters for nafion. Ind. Eng. Chem. Fund. 23, 234–243. https://doi.org/10.1021/i100014a017.

29. Khalid, H., Najibah, M., Park, H.S., Bae, C., and Henkensmeier, D. (2022). Properties of anion exchange membranes with a focus on water electrolysis. Membranes 12, 989. https://doi.org/10.3390/membranes12100989.

30. Li, D., Motz, A.R., Bae, C., Fujimoto, C., Yang, G., Zhang, F., Ayers, K.E., and Kim, Y.S. (2021). Durability of anion exchange membrane water electrolyzers. Energy Environ. Sci. 14, 3393–3419. https://doi.org/10.1039/D0EE04086J.

31. Dickinson, E.J.F., Limon-Petersen, J.G., and Compton, R.G. (2011). The electroneutrality approximation in electrochemistry. J. Solid State Electrochem. 15, 1335–1345. https://doi.org/10.1007/s10008-011-1323-x.

32. Gao, K.W., Yu, X., Darling, R.M., Newman, J., and Balsara, N.P. (2022). Increased Donnan exclusion in charged polymer networks at high salt concentrations. Soft Matter 18, 282–292. https://doi.org/10.1039/D1SM01511G.

33. Blommaert, M.A., Verdonk, J.A.H., Blommaert, H.C.B., Smith, W.A., and Vermaas, D.A. (2020). Reduced ion crossover in bipolar membrane electrolysis via increased current density, molecular size, and valence. ACS Appl. Energy Mater. 3, 5804–5812. https://doi.org/10.1021/acsaem.0c00687.

34. Bui, J.C., Digdaya, I., Xiang, C., Bell, A.T., and Weber, A.Z. (2020). Understanding multi-ion transport mechanisms in bipolar membranes. ACS Appl. Mater. Interfaces 12, 52509–52526. https://doi.org/10.1021/acsami.0c12686.

35. Paddison, S.J., and Paul, R. (2002). The nature of proton transport in fully hydrated Nafion®. Phys. Chem. Chem. Phys. 4, 1158–1163. https://doi.org/10.1039/b109792j.

36. Adam, L.C., and Gordon, G. (1999). Hypochlorite ion decomposition: effects of temperature, ionic strength, and chloride ion. Inorg. Chem. 38, 1299–1304. https://doi.org/10.1021/ic980020q.

37. Lindquist, G.A., Oener, S.Z., Krivina, R., Motz, A.R., Keane, A., Capuano, C., Ayers, K.E., and Boettcher, S.W. (2021). Performance and durability of pure-water-fed anion exchange membrane electrolyzers using baseline materials and operation. ACS Appl. Mater. Interfaces 13, 51917–51924. https://doi.org/10.1021/acsami.1c06053.

38. Krivina, R.A., Lindquist, G.A., Beaudoin, S.R., Stovall, T.N., Thompson, W.L., Twight, L.P., Marsh, D., Grzyb, J., Fabrizio, K., Hutchison, J.E., and Boettcher, S.W. (2022). Anode catalysts in anion-exchange-membrane electrolysis without supporting electrolyte: conductivity, dynamics, and ionomer degradation. Adv. Mater. 34, e2203033. https://doi.org/10.1002/adma.202203033.

39. Rossi, R., Hall, D.M., Shi, L., Cross, N.R., Gorski, C.A., Hickner, M.A., and Logan, B.E. (2021). Using a vapor-fed anode and saline catholyte to manage ion transport in a proton exchange membrane electrolyzer. Energy Environ. Sci. 14, 6041–6049. https://doi.org/10.1039/D1EE02265B.

40. Bernt, M., Hartig-Weiß, A., Tovini, M.F., El-Sayed, H.A., Schramm, C., Schröter, J., Gebauer, C., and Gasteiger, H.A. (2020). Current challenges in catalyst development for PEM water electrolyzers. Chem. Ing. Tech. 92, 31–39. https://doi.org/10.1002/cite.201900101.

41. Sun, S., Shao, Z., Yu, H., Li, G., and Yi, B. (2014). Investigations on degradation of the long-term proton exchange membrane water electrolysis stack. J. Power Sources 267, 515–520. https://doi.org/10.1016/j.jpowsour.2014.05.117.

42. IRENA (2020). Green hydrogen cost reduction: scaling up electrolysers to meet the 1.5oC climate goal. International Renewable Energy Agency (IRENA). https://www.irena.org/-/media/Files/IRENA/Agency/Publication/2020/Dec/IRENA_Green_hydrogen_cost_2020.pdf.

43. Suermann, M., Bensmann, B., and Hanke-Rauschenbach, R. (2019). Degradation of proton exchange membrane (PEM) water electrolysis cells: looking beyond the cell voltage increase. J. Electrochem. Soc. 166, F645–F652. https://doi.org/10.1149/2.1451910jes.

44. Mayyas, A.T., Ruth, M.F., Pivovar, B.S., Bender, G., and Wipke, K.B. (2019). Manufacturing cost analysis for proton exchange membrane water electrolyzers. Technical report (National Renewable Energy Lab). https://doi.org/10.2172/1557965.

45. Standard Methods Committee of the American Public Health Association, American Water Works Association, and Water Environment Federation. (2022). 4500-Cl chlorine (residual). In Standard Methods for the Examination of Water and Wastewater (APHA Press).

46. Tarvin, D., Todd, H.R., and Buswell, A.M. (1934). The determination of free chlorine. J. Am. Water Works Assoc. 26, 1645–1662. https://doi.org/10.1002/j.1551-8833.1934.tb14393.x.

Supplemental information

Hydrogen production with seawater-resilient

bipolar membrane electrolyzers

Daniela H. Marin, Joseph T. Perryman, McKenzie A. Hubert, Grace A. Lindquist, Lihaokun Chen, Ashton M. Aleman, Gaurav A. Kamat, Valerie A. Niemann, Michaela Burke Stevens, Yagya N. Regmi, Shannon W. Boettcher, Adam C. Nielander, and Thomas F. Jaramillo
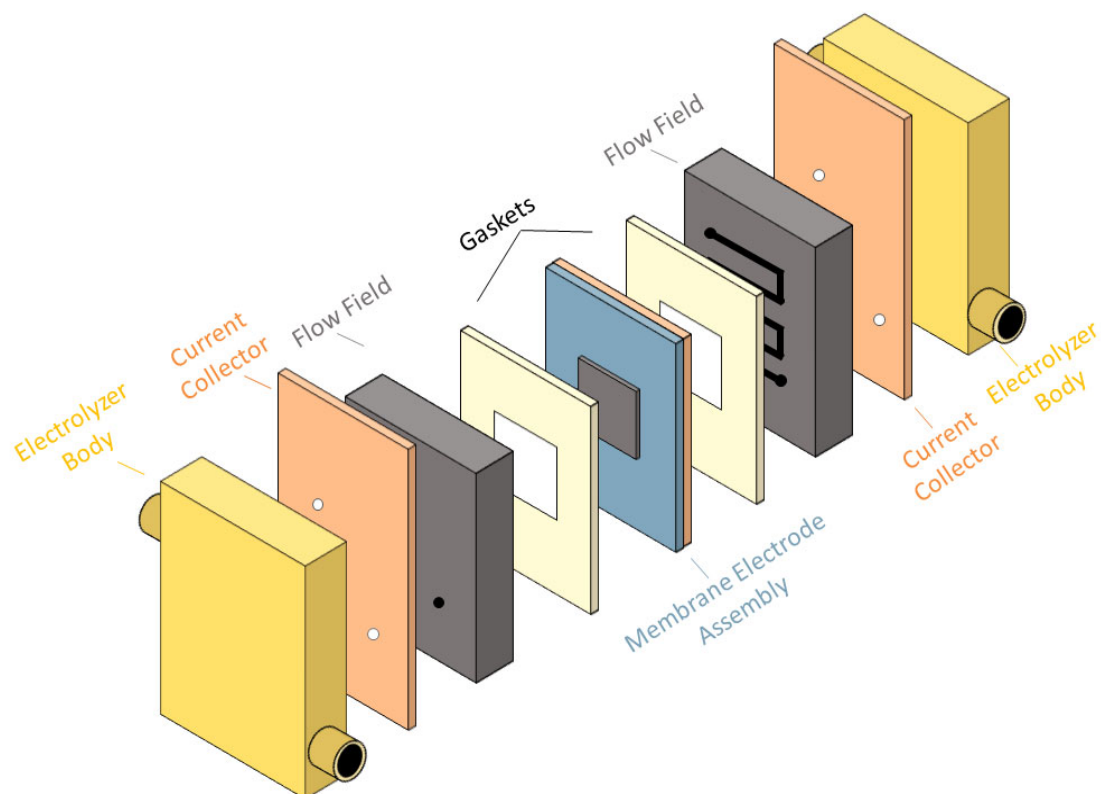
Supplemental Items

Figure S1. Schematic depicting the architecture of an assembled BPMWE. PEMWE architectures are similar but with a monopolar CEL membrane instead of the bipolar membrane in the membrane electrode assembly. AEMWE architectures were also similar but with a monopolar AEL membrane instead of the bipolar membrane. Briefly, the AEMWE was constructed in a similar manner to the BPMWE (see methods), with the following exceptions: 1) the ionomer in the cathode catalyst ink and ionomer overlayer was PiperION rather than Nafion, 2) only one layer of PiperION was used to separate the anode from the cathode rather than the CEL/AEL combination used in the BPMWE.
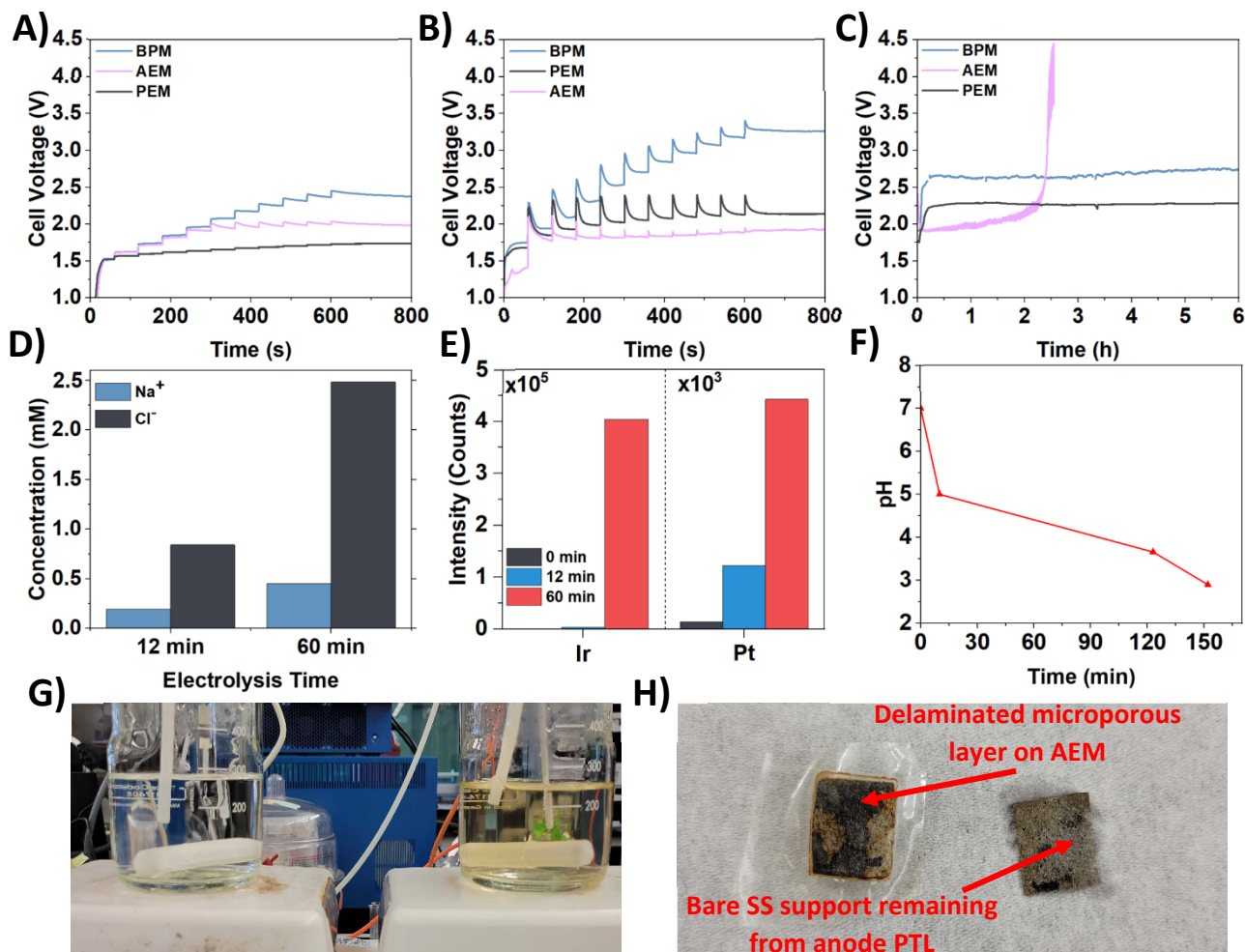
Figure S2. Performance and failure analysis of AEMWEs. (A) Voltage-time behavior during CP1 stepped chronopotentiometry with DI H_2O as the cathode feed for a BPMWE (**blue**), AEMWE (**pink**), and PEMWE (**black**). (B) Voltage traces during CP1 stepped chronopotentiometry with aqueous 0.5 M NaCl as the cathode feed for a BPMWE (**blue**), AEMWE (**pink**), and PEMWE (**black**). (C) 6 hour-long galvanostatic measurement (j=250 mA cm^{-2}) under asymmetric (aqueous 0.5 M NaCl as the cathode feed, DI water anode feed) for all three electrolyzer constructs. The AEMWE was stopped upon reaching a cell voltage of 4.5 V. (D) Na$^+$ (**blue**) and Cl$^-$ (**black**) concentrations in the anode feed of an AEMWE at various points in time during asymmetric mode electrolysis (0.5 M NaCl$_{aq}$ fed to cathode) at 250 mA cm^{-2}. (E) Relative ICP-MS intensity for dissolved Pt and Ir in the anode feed of an AEMWE at various points in time during asymmetric mode electrolysis (0.5 M NaCl$_{aq}$ fed to cathode) at 250 mA cm^{-2}. (F) pH in the anode chamber over time for the AEMWE shown in panel C. (G) Cathode feed (**left**) and anode feed (**right**) after 158 minutes of electrolysis with asymmetric 0.5 M NaCl$_{aq}$ cathode feed for an AEMWE, illustrating the discoloration of the anode feed from dissolved metals like Fe that were present from the PTL. **H)** AEM/anode interface side of the AEM (left) after 158 minutes of 0.5 M NaCl electrolysis with an AEMWE, alongside the corresponding anode PTL, illustrating the extreme loss of the stainless-steel microporous layer over the course of electrolysis. See methods for description of CP1 electrochemical routine.
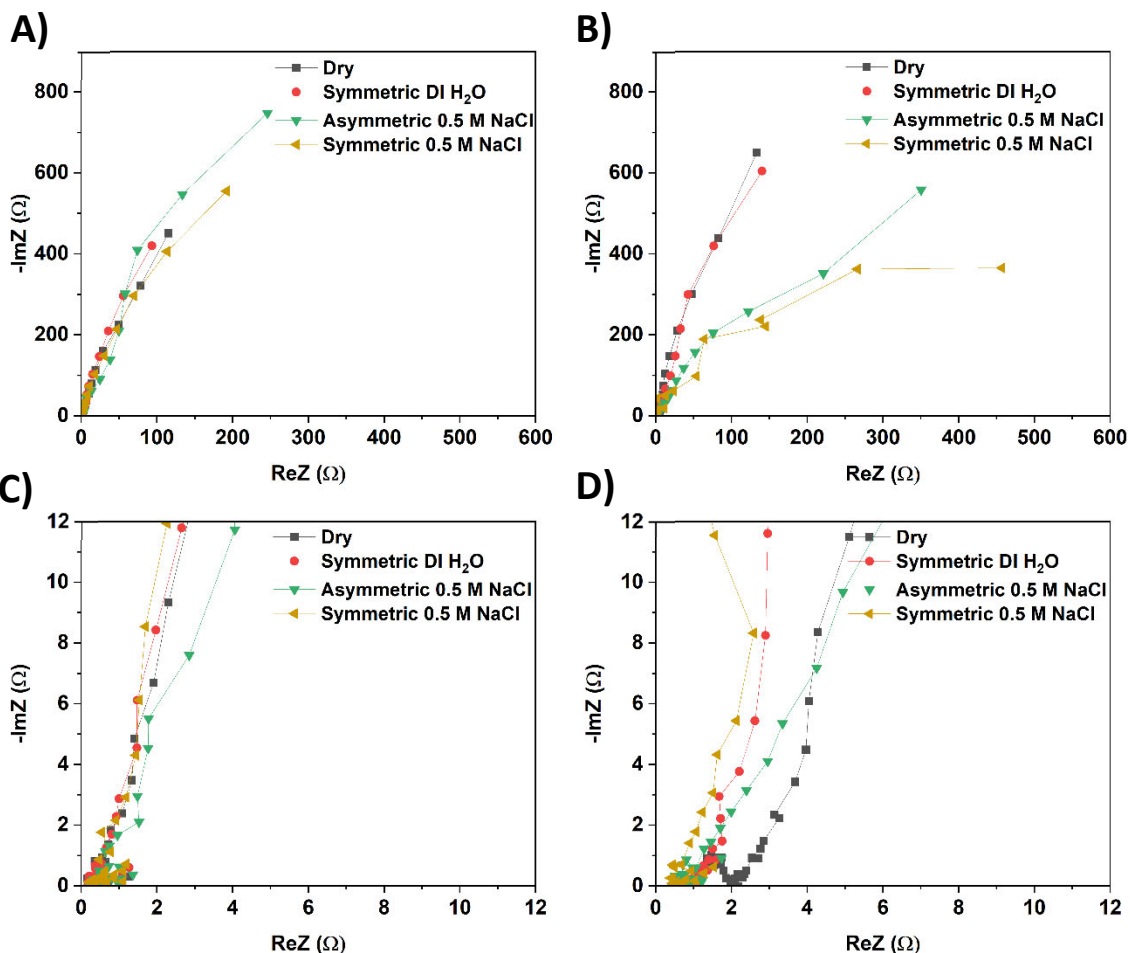
Figure S3. Zero-current impedance analysis. Full 0 mA GEIS Nyquist plots under different electrolyte conditions for the PEMWE (A) and the BPMWE (B). Zoomed-in perspectives of the spectra in (A) and (B), illustrating the high-frequency intercepts, are shown below for the PEMWE (C) and for the BPMWE (D). All 0 mA GEIS experiments shown were performed with a 20 µA sinus amplitude. See Note S4 and methods for additional details.
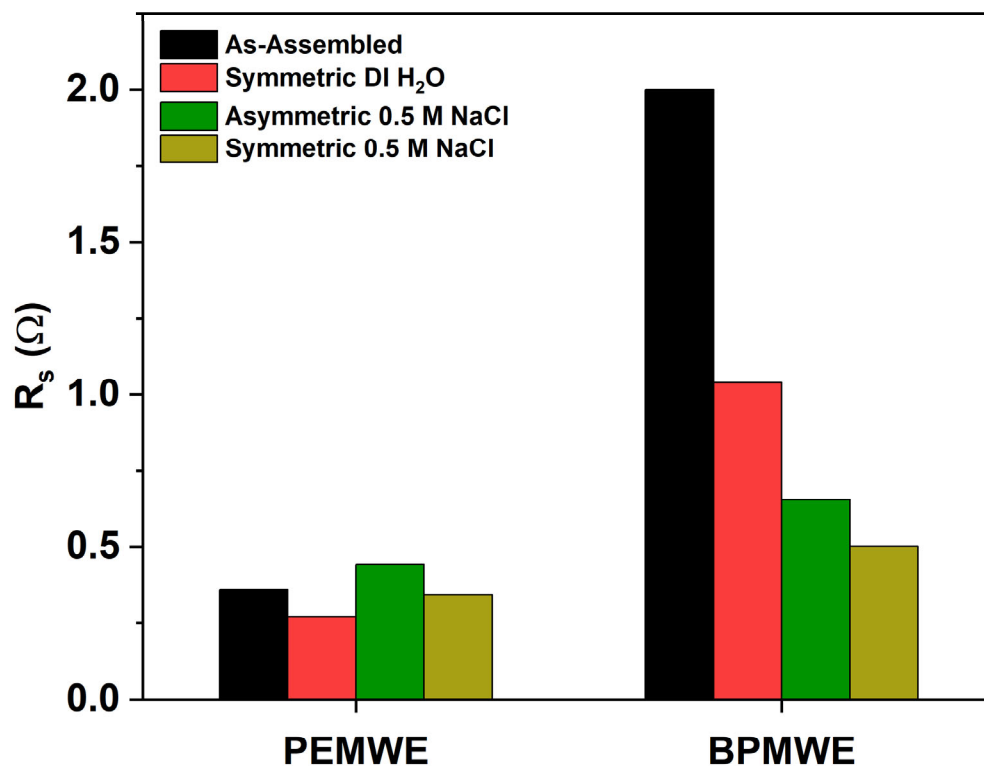
Figure S4. Series resistance comparison. R_s values with varied electrolyte conditions as extracted from the PEMWE and BPMWE 0 mA GEIS experiments shown in **Fig. S3**, highlighting a significant dependence on total membrane resistance in the BPMWE on electrolyte conditions, compared to a relative insensitivity in the case of the PEMWE. We note that in both electrolyzers, extracted resistances at 0 mA mirror those of the high-current experiments that are represented in **Fig. S5** and **Fig. S6**, indicating minimal dependence of R_s on current density in the ranges studied here. See Note S4 for additional discussion.
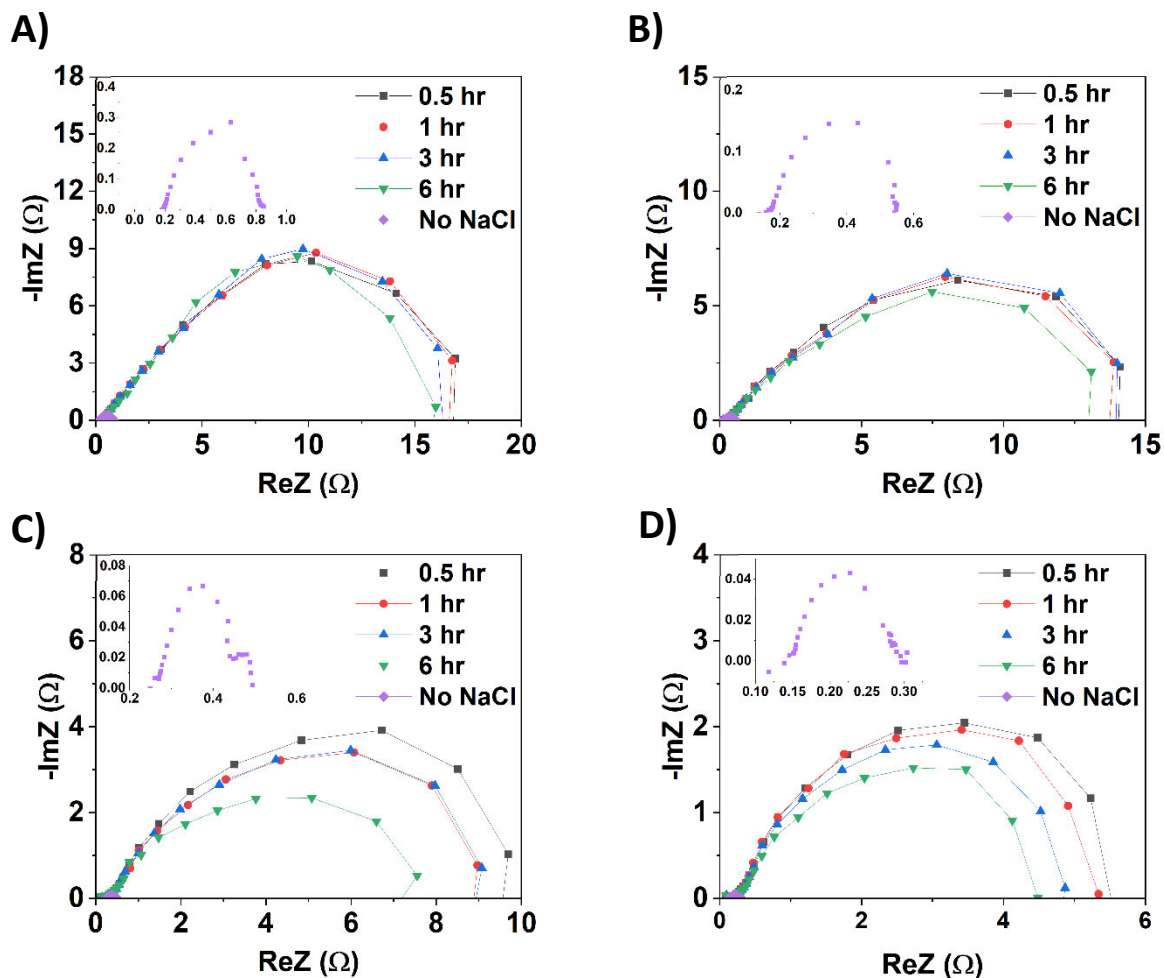
Figure S5. Electrolyte- and time-dependent PEMWE impedance spectroscopy. Average GEIS spectra scanned from 300 kHz to 20 mHz before (**Purple**) and at several timepoints after the addition of 0.5 M NaCl to the cathode feed in a PEMWE at applied current densities of (A) 50 mA cm^{-2}, (B) 100 mA cm^{-2}, (C) 250 mA cm^{-2}, and (D) 500 mA cm^{-2}. Scans represent the average spectra from no less than three replicate experiments. Insets are a zoomed in depiction having the same axis labels of the averaged result of GEIS at each corresponding current density prior to adding aqueous 0.5 M NaCl to the cathode feed ("No NaCl"). See Note S4 and methods for additional details.
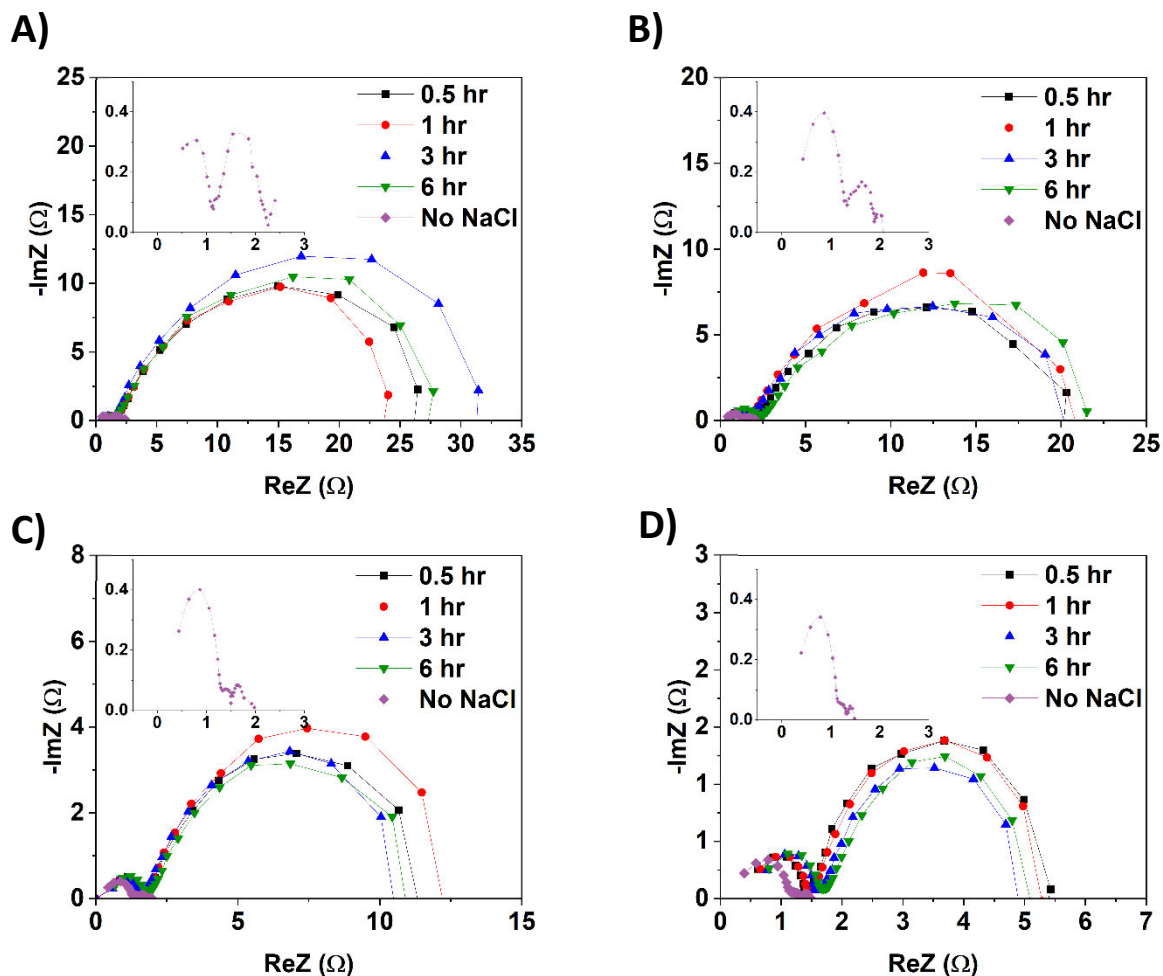
Figure S6. Electrolyte- and time-dependent BPMWE impedance spectroscopy Average GEIS spectra scanned from 300 kHz to 20 mHz before (**Purple**) and at several timepoints after the addition of 0.5 M NaCl to the cathode feed in a BPMWE at applied current densities of (A) 50 mA cm^{-2}, (B) 100 mA cm^{-2}, (C) 250 mA cm^{-2}, and (D) 500 mA cm^{-2}. Scans represent the average spectra from no less than three replicate experiments. Insets are a zoomed in depiction having the same axis labels of the averaged result of GEIS at each corresponding current density prior to adding 0.5 M NaCl to the cathode feed ("No NaCl"). In these plots, the higher frequency left semi-circle has been assigned to water dissociation while the lower frequency right semi-circle corresponds to charge transfer. See Note S4 and methods for additional details.
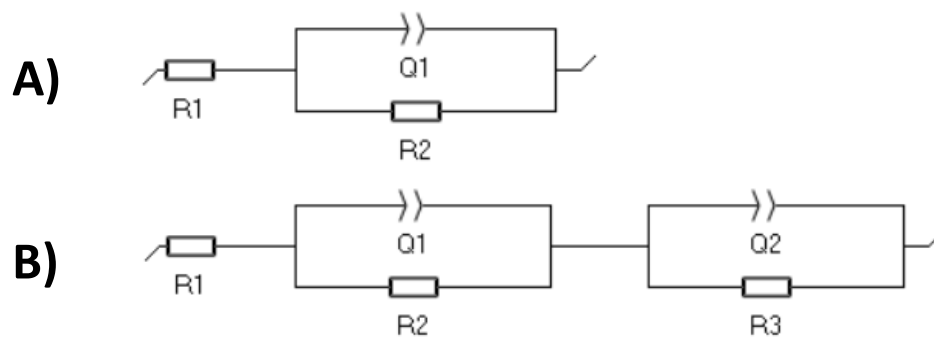
Figure S7. **Equivalent circuits that were used for all GEIS fitting in this work.** (A) PEMWE equivalent circuit where R1 corresponds to R_s and R_2 corresponds to R_{CT} and (B) BPMWE equivalent circuit where R1 corresponds to R_s, R_2 corresponds to R_{CT}, and R_3 corresponds to R_{WD}. Constant phase elements are used in all cases to account for non-ideal capacitive behavior of the electric double layer and WD catalyst.
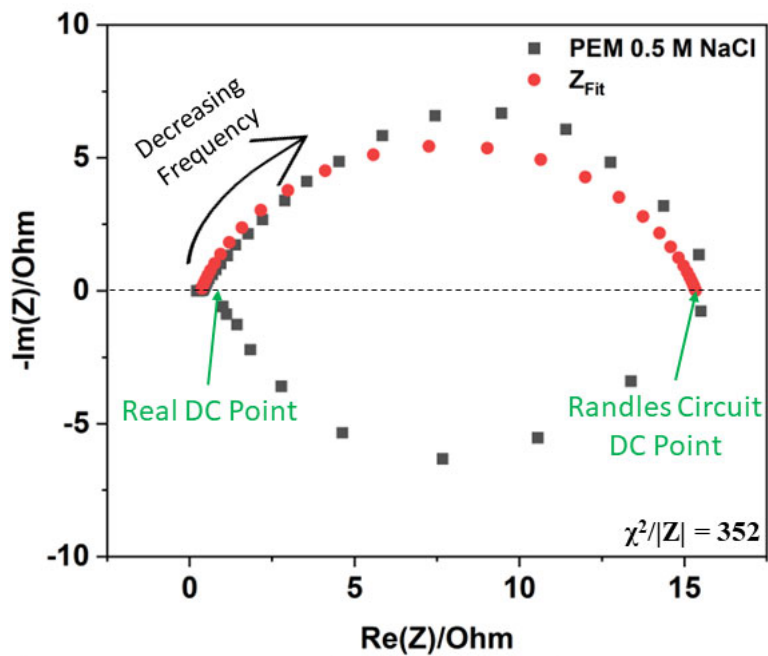
Fit Parameter	Value	Unit
R1 (R_s)	0.257	Ohm
Q1 (C_{DL})	.02	F.s^(a-1)
A1	0.769	
R2 (R_{CT})	15.3	Ohm

Figure S8. **Randles circuit model comparison to real PEMWE impedance.** Nyquist plot showing real and imaginary components of PEMWE impedance (**black**) at 250 mA cm^{-2} with aqueous 0.5 M NaCl added to the cathode feed, scanned in the range 300 kHz→1 mHz, illustrating a significant low-frequency inductive element that cannot be modeled (**red**) with a Randles cell equivalent circuit. Highlighted in green are the **right)** DC point that would be erroneously extracted from using a Randles equivalent circuit to model the system versus the **left)** real DC point that agrees with the measured PEMWE cell current and voltage. Corresponding table with fit parameters also shown: R1 and R2 represent series and charge-transfer resistance, respectively, while Q1 and A1 represent a constant phase element and its corresponding exponential parameter that describes deviation from "ideal" capacitive behavior, respectively. See Note S4 and methods for additional details.
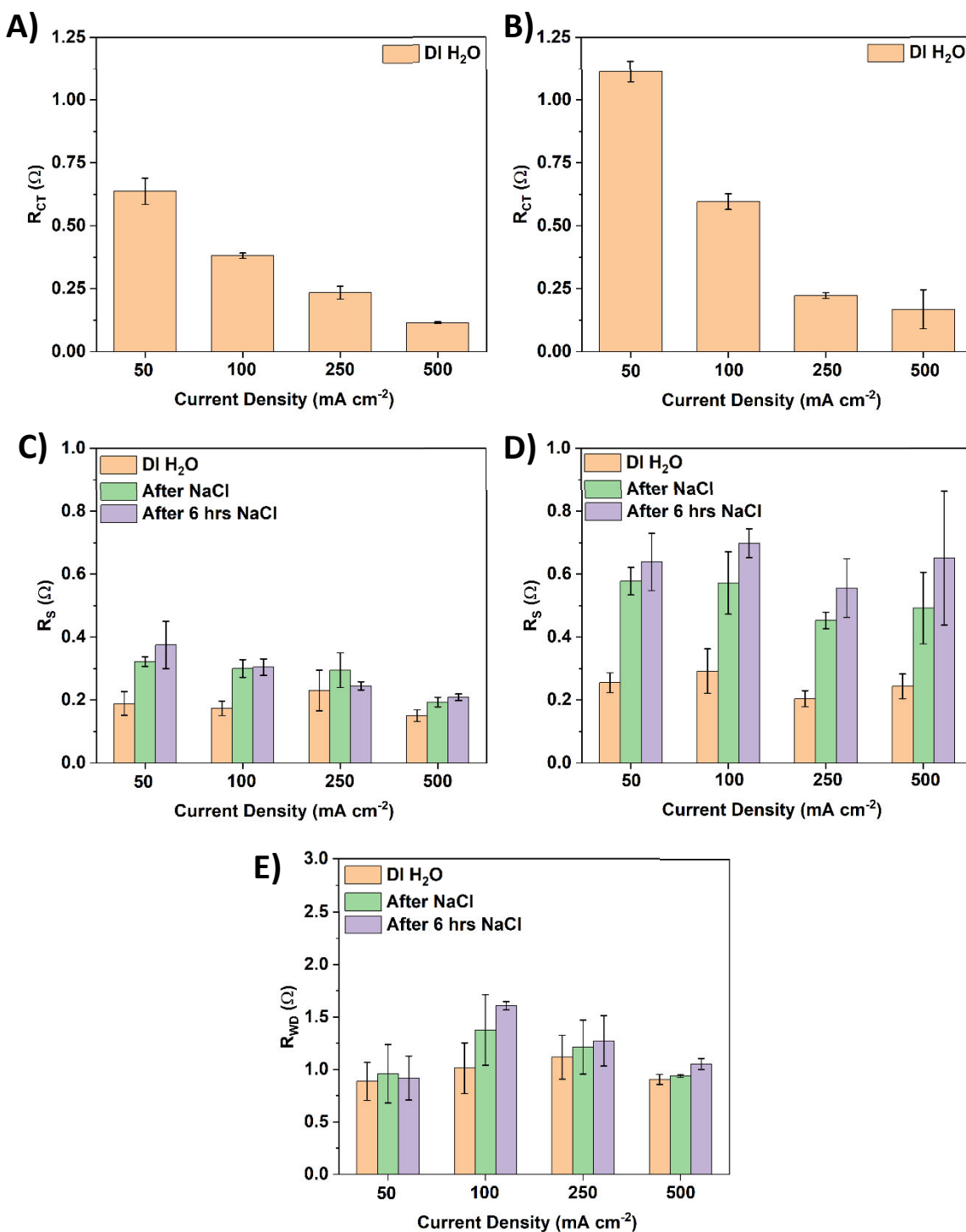
Figure S9. Average resistance values during PEMWE and BPMWE operation. GEIS during chronopotentiometry at 50-500 mA cm^{-2} before adding NaCl to the cathode feed (**orange**), immediately after adding 0.5 M NaCl to the cathode feed (**green**), and after 6 hours of electrolysis with 0.5 M NaCl in the cathode feed (**purple**). (A) PEMWE charge-transfer resistances, (B) BPMWE charge-transfer resistances, (C) PEMWE series resistances, (D) BPMWE series resistances, and (E) BPMWE water-dissociation resistances. Error bars represent a single standard deviation taken from no less than three replicate experiments.
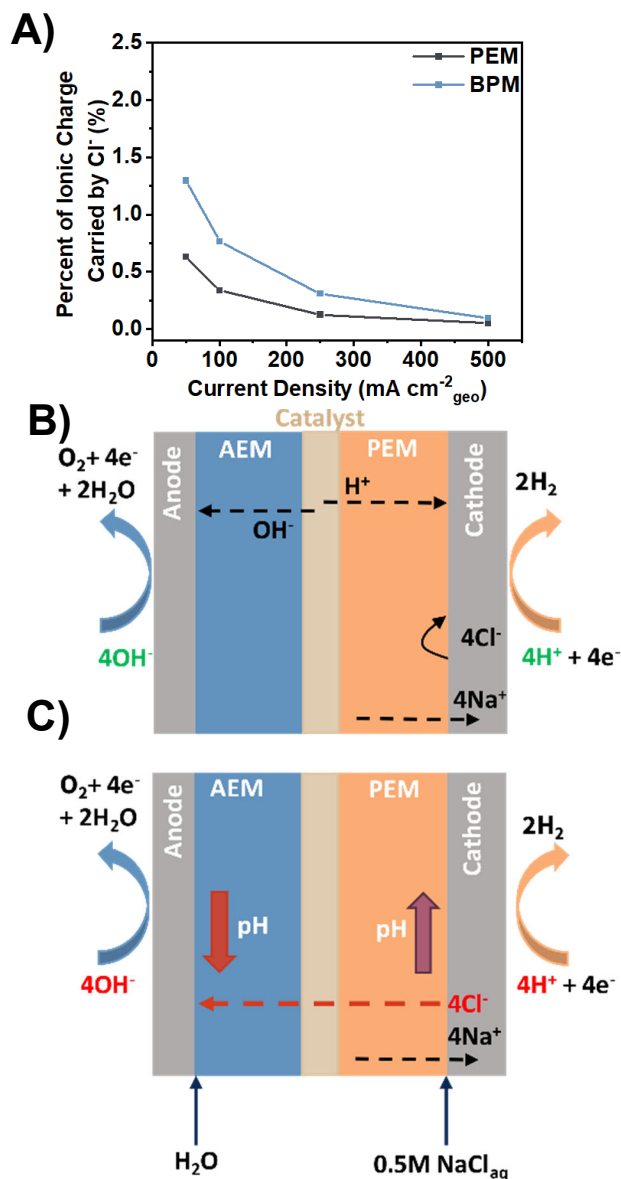
Figure S10. Ionic current selectivity during PEMWE and BPMWE operation. (A) Percent of total ionic charge carried by Cl⁻ migration during BPMWE (**blue**) and PEMWE (**black**) as a function of applied current density under asymmetric operating conditions (0.5 M NaCl$_{aq}$ as the cathode feed; DI H$_2$O as the anode feed) [See Note S2]. (B) Schematic of ion transport for BPMWE architecture, where H⁺ and OH⁻ that are consumed at the cathode and anode, respectively, are ideally replenished by the H⁺ and OH⁻ generated by water dissociation catalysis. In the ideal case, Na⁺ is suppressed by the direction of the electric field, and Cl⁻ by Donnan exclusion. (C) Schematic of an alternative, deleterious mechanism of carrying current through this system involving Cl⁻ migration to the anode which must proceed in lieu of a WD event (BPMWE) or in lieu of a H⁺ crossover event (PEMWE), leading to pH variations at both electrodes.
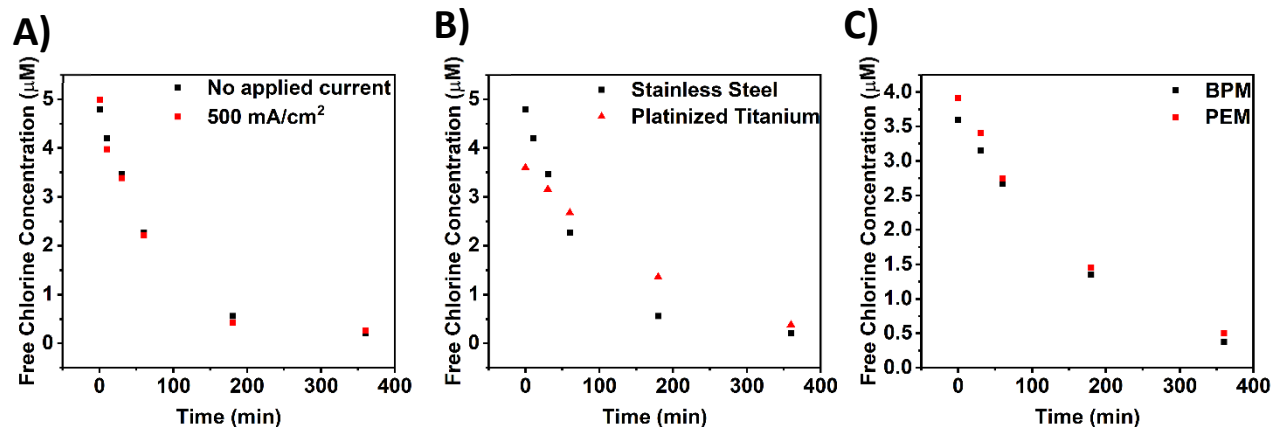
Figure S11. Measurements of free chlorine degradation over time. DI water was circulated in the cathode reservoir and a solution of aqueous NaOCl [Sigma Aldrich, reagent grade] diluted to 3.5-5 µM was circulated to the anode reservoir chamber. The concentration of free chlorine in the anode chamber was monitored for 6 hours at 50 °C. (A) Free chlorine concentration in the anode reservoir over time using BPMWE architecture with no applied current (**black**) compared to with 500 mA cm^{-2} applied current (**red**) using stainless steel PTL in both cases, (B) Free chlorine concentration over time using BPMWE architecture when PTL material is stainless steel (**black**) compared to a platinized titanium PTL (**red**) at open circuit voltage, and (C) Free chlorine concentration over time using BPM (**black**) and PEM (**red**) in water electrolyzer. First-order rate constants are in the same order of magnitude (10^{-4} s^{-1}) indicating that neither applied potential, PTL material, or membrane type significantly affect hypochlorite degradation kinetics.
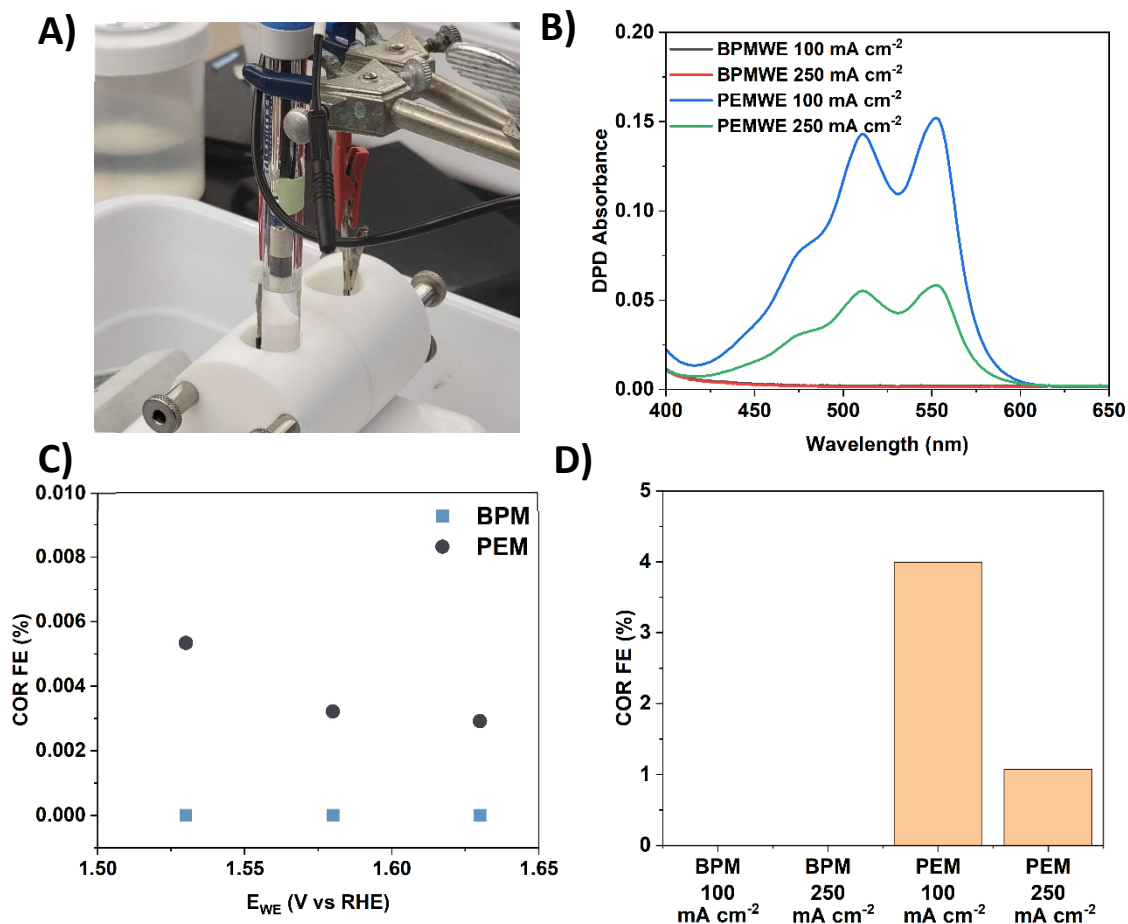
Figure S12. Three-electrode measurements. (A) Image of the PTFE H-Cell that was used to evaluate "simulated" electrolyzer anode environments in three-electrode configurations. (B) UV-Vis spectra illustrating the absorbance response from the DPD test (see methods section), indicating the presence of free chlorine dissolved in electrolyte after passing 20 C of charge. (C) COR Faradaic efficiency (see Note S1) for simulated BPM (**blue**) anode environments (1 M KOH, 0.5 M NaCl, PiperION ionomer overlayer) and simulated PEM (**black**) anode environments (0.5 M H_2SO_4, 0.5 M NaCl, Nafion ionomer overlayer) as a function of applied potential. (D) COR Faradaic efficiency for simulated BPM (**blue**) anode environments and simulated PEM (**black**) anode environments at geometric current densities analogous to those observed in MEA electrolysis, highlighting both the lack of free chlorine generation at BPM anode environments, as well as the apparent decrease in COR efficiency as current density increases for the PEM. All experiments were performed with aq. 0.5 M NaCl as the anolyte, dissolved in either 1 M NaOH (simulated BPM experiments) or 0.5 M H_2SO_4 (simulated PEM experiments), thereby maximizing Cl$^-$ access to the IrO_x catalyst and informing whether either electrolyzer construct can feasibly operate with seawater on both sides of the device.
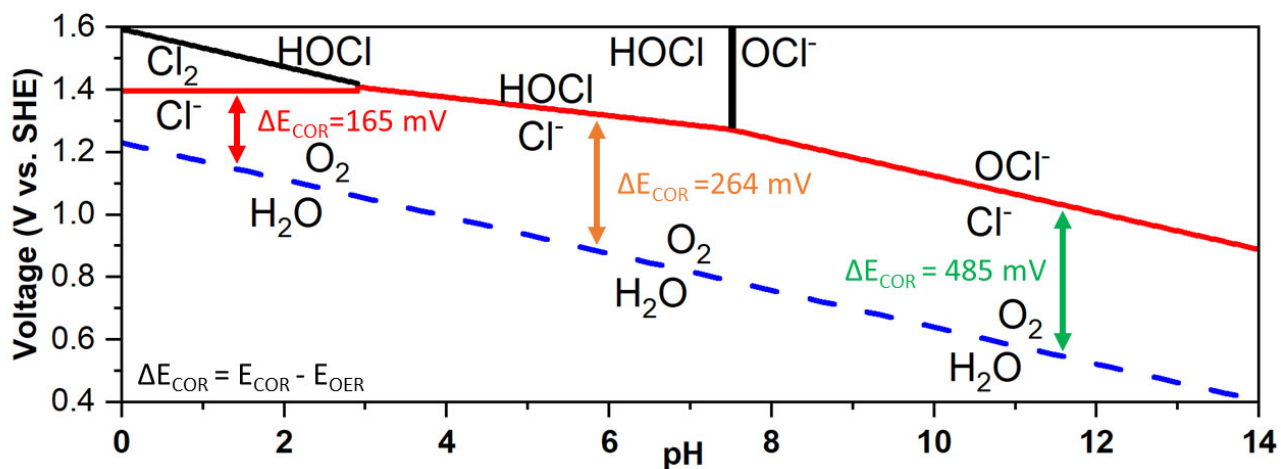
Figure S13. Chlorine Pourbaix diagram. Pourbaix diagram illustrating a subset of relevant thermodynamic potentials for oxidation reactions involving H_2O and Cl^-, highlighting the potentials beyond which relevant corrosive COR pathways can become competitive with OER (ΔE_{COR}) under various pH conditions.
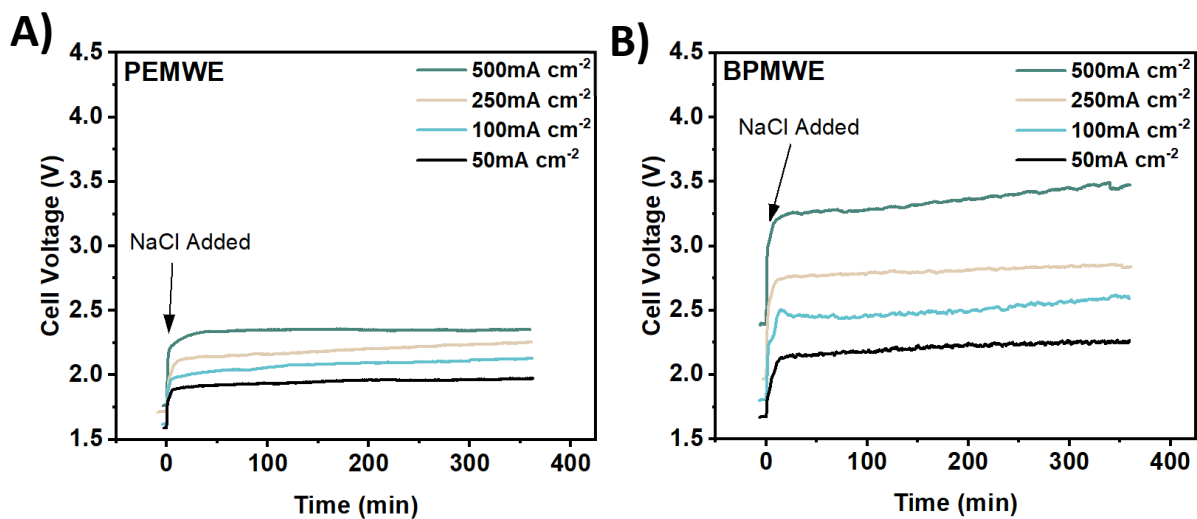
Figure S14. PEMWE and BPMWE voltage stability over time. Representative V-t behavior over six hours of electrolysis at 50, 100, 250, and 500 mA cm^{-2} with 0.5 M NaCl$_{aq}$ fed to the cathode side of a (A) PEM electrolyzer and (B) BPM electrolyzer.
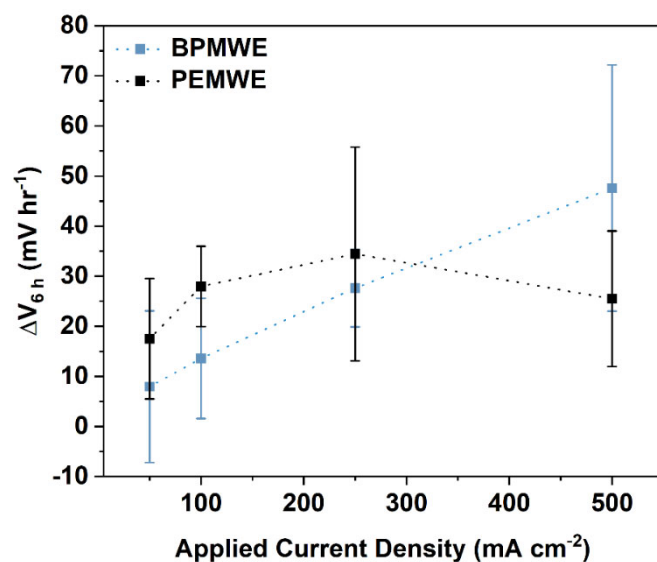
Figure S15. Current dependence of PEMWE and BPMWE voltage stability. Voltage degradation rates $(\Delta V_{6\,h})$ at each current density tested for BPMWEs (**blue**) and PEMWEs (**black**) after adding 0.5 M NaCl$_{aq}$ to the cathode feed (see **Fig. S14**). This voltage degradation is consistent with membrane degradation at the anode-AEM interface that drives increased series resistance over time (see **Fig. S9**), as well as generation of oxidizing chlorine species at the PEMWE anode (see **Fig. S17**). Fit lines added to guide the eye and do not represent additional data. Error bars represent standard deviations taken from no less than three replicate experiments.
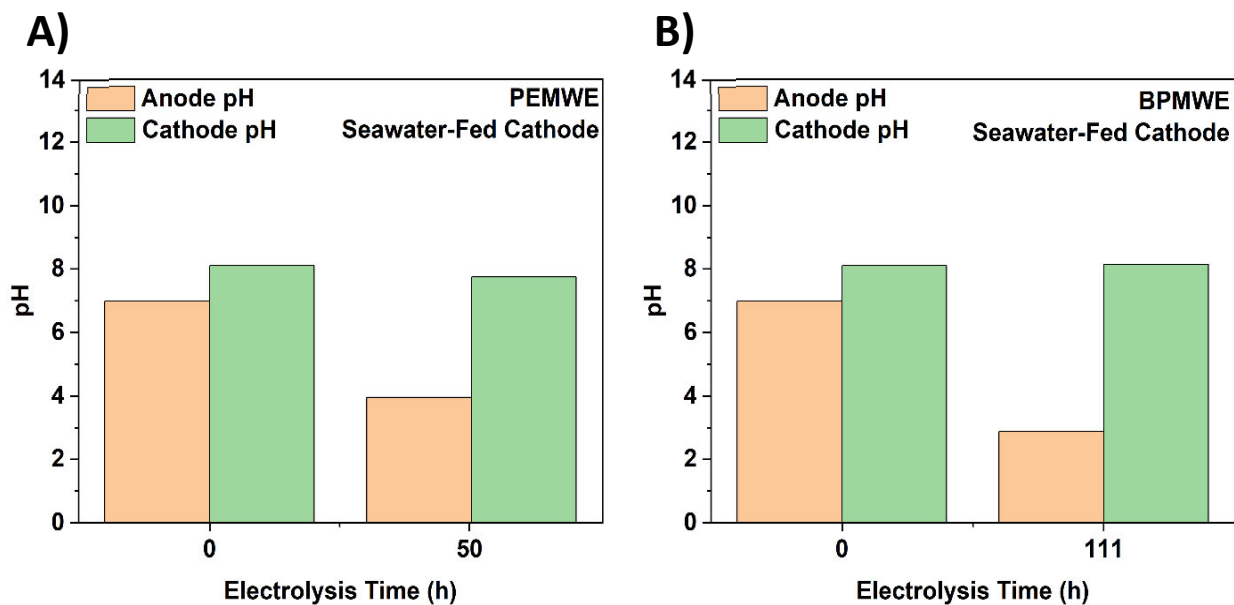
Figure S16. PEMWE and BPMWE pH over time during seawater electrolysis. Anode feed (**orange**) and cathode feed (**green**) pH at the beginning and end of seawater electrolysis at 250 mA cm^{-2} in a (A) PEMWE with seawater on the cathode side and DI H$_2$O on the anode side and (B) BPMWE with seawater on the cathode side and DI H$_2$O on the anode side, illustrating the gradual acidification of the bulk anode feed over time and the relatively unchanged bulk cathode feed pH over time. Note that at t = 0, the pH of initially ultrapure DI water in the anode chamber could not be measured reliably using an electronic pH probe, and thus the pH was measured using high resolution pH paper (Hydrion, pH 5.5-8.0 test strips).
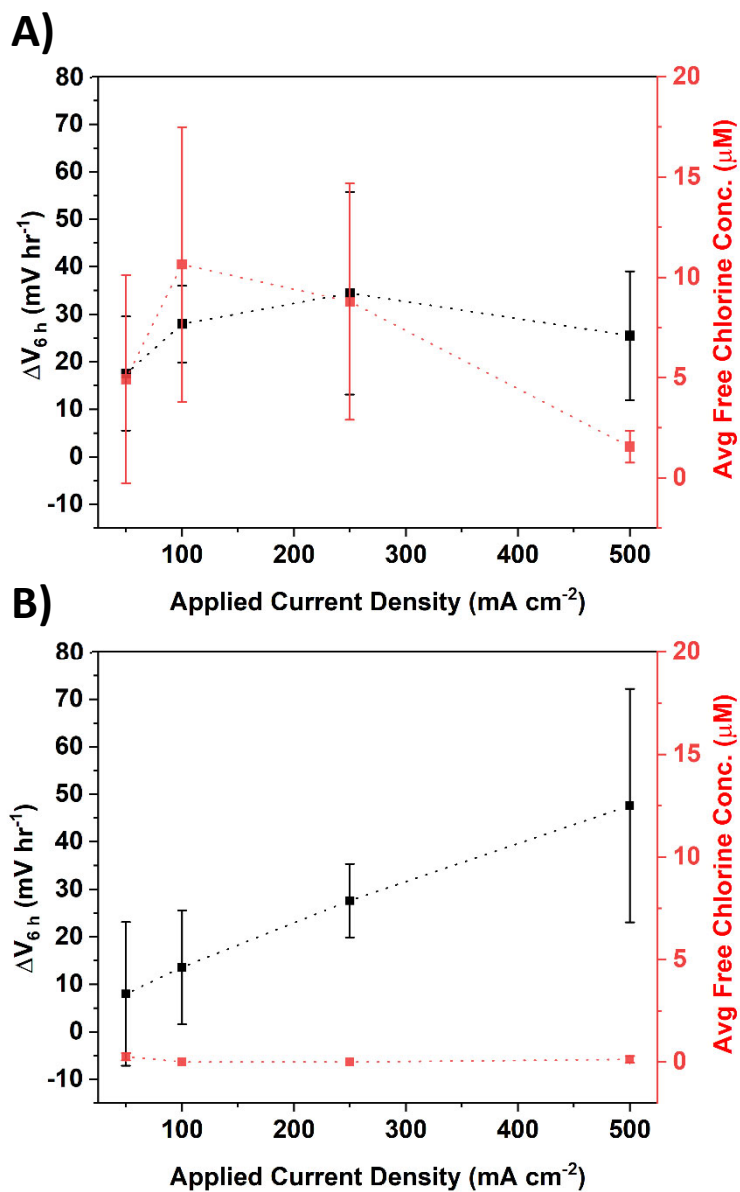
Figure S17. Free chlorine correlation with PEMWE and BPMWE voltage stability. Voltage degradation rates over the course of 6 hours of constant-current electrolysis (**black**) compared to free chlorine concentration accumulated after 6 hours of constant-current electrolysis (**red**) at each current density tested for (A) PEMWEs and (B) BPMWEs after adding 0.5 M $NaCl_{aq}$ to the cathode feed. Error bars in all cases represent a single standard deviation extracted from no less than three replicate experiments. Fit lines added to guide the eye and do not represent additional data.

Figure S18. PEMWE XPS analysis. XPS survey scans illustrating the surface composition of PEMWE electrodes after seawater electrolysis experiments, including: (A) anode after symmetric seawater electrolysis, (B) anode after asymmetric seawater electrolysis, (C) cathode after symmetric seawater electrolysis, and (D) cathode after asymmetric seawater electrolysis. Significant Mg deposition in (C) is consistent with the additional contribution by Mg(OH)$_2$ precipitation to the immediate voltage loss observed in **Figure 5B** of the main manuscript.
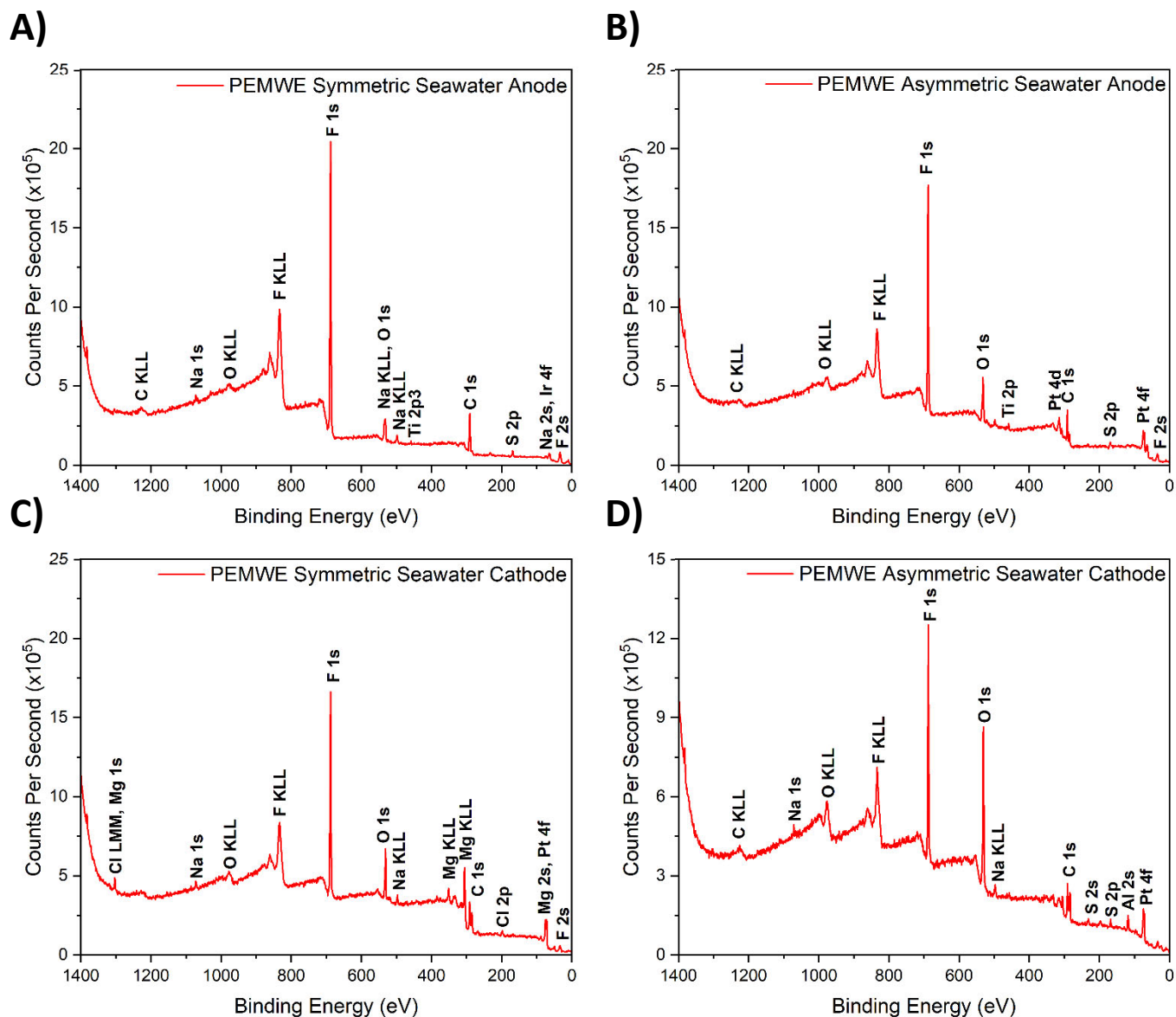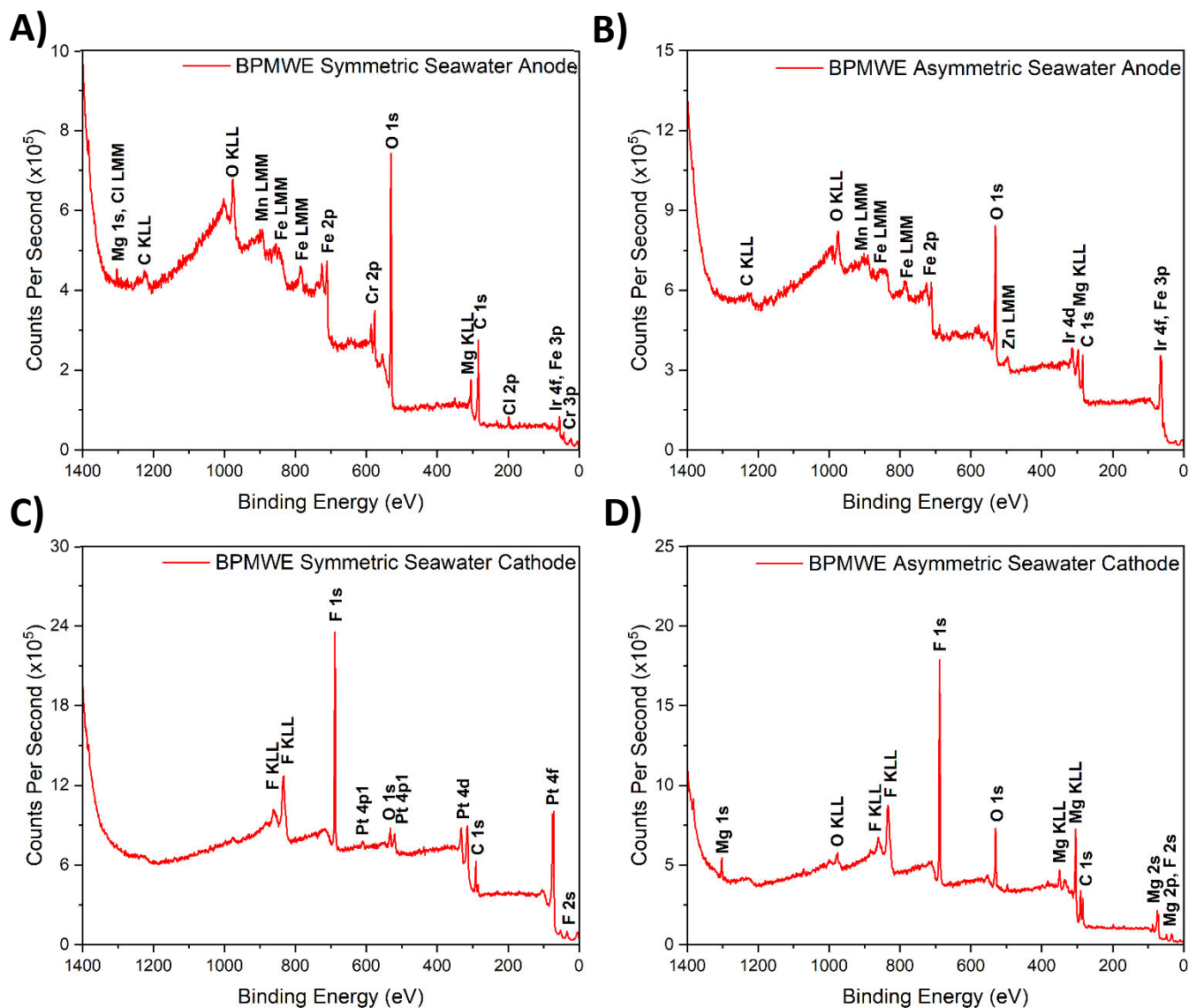
Figure S19. BPMWE XPS analysis. XPS survey scans illustrating the surface composition of BPMWE electrodes after seawater electrolysis experiments, including: (A) anode after symmetric seawater electrolysis, (B) anode after asymmetric seawater electrolysis, (C) cathode after symmetric seawater electrolysis, and (D) cathode after asymmetric seawater electrolysis. Significant Mg deposition in (D) is consistent with the additional contribution by $Mg(OH)_2$ precipitation to the gradual voltage loss observed in **Figure 5A** of the main manuscript, although it's absence in (C) indicates that $Mg(OH)_2$ did not play a significant role in the BPMWE's accelerated failure during symmetric seawater electrolysis. Rather, we attribute the diminished Ir signal in (A) compared to (B) to an increased rate of stainless steel corrosion, which we attribute to the locally more acidic pH conditions. We believe these local pH conditions during symmetric seawater electrolysis led to catalyst detachment from the BPM anode.

Figure S20. Pre-electrolysis PEMWE and BPMWE electrode morphology. SEM images showing the surface morphology of PEMWE/BPMWE electrodes before seawater electrolysis experiments, including: (A) PEMWE/BPMWE cathode, (B) BPMWE anode, and (C) PEMWE anode.
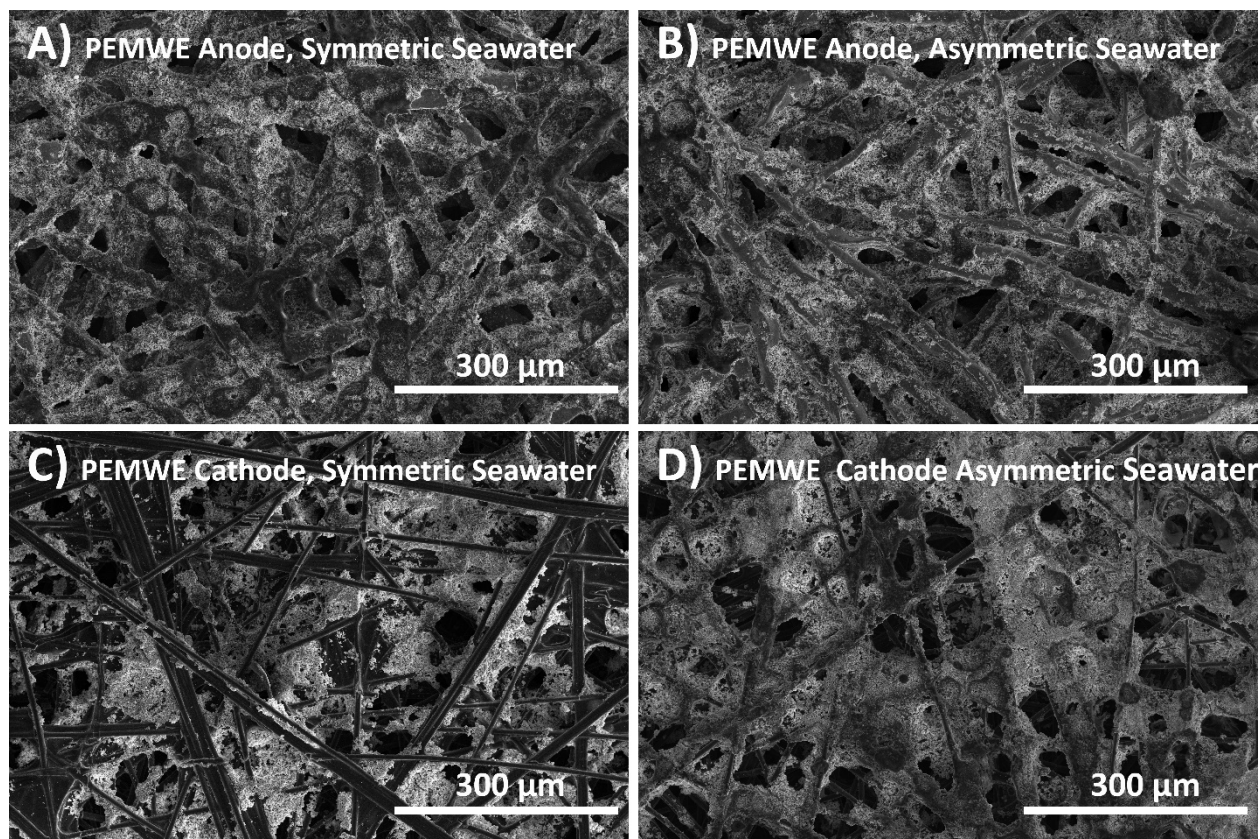
Figure S21. Post-electrolysis PEMWE electrode morphology. SEM images showing the surface morphology of PEMWE electrodes after seawater electrolysis experiments, including: (A) anode after symmetric seawater electrolysis, (B) anode after asymmetric seawater electrolysis, (C) cathode after symmetric seawater electrolysis, and (D) cathode after asymmetric seawater electrolysis. It appears from these SEM images that catalyst loss as observed in (C) after three minutes of symmetric seawater electrolysis was greater than catalyst loss is seen under asymmetric seawater electrolysis (D).
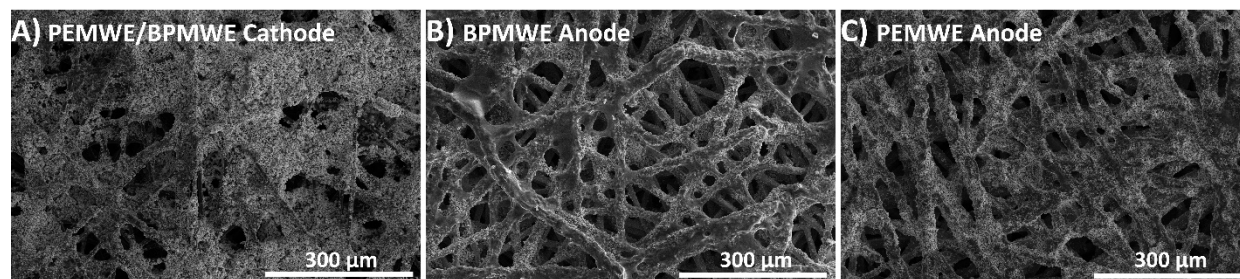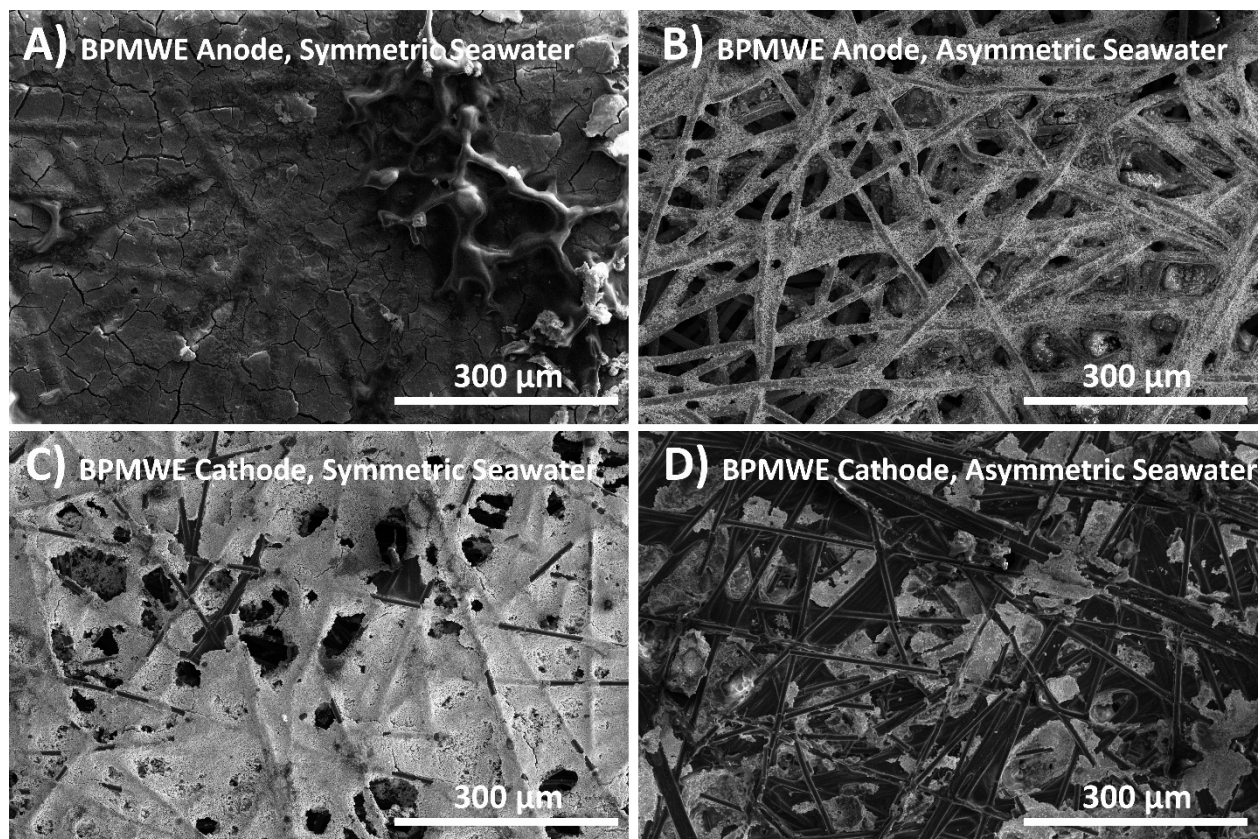
Figure S22. Post-electrolysis BPMWE electrode morphology. SEM images showing the surface morphology of BPMWE electrodes after seawater electrolysis experiments, including: (A) anode after symmetric seawater electrolysis, (B) anode after asymmetric seawater electrolysis, (C) cathode after symmetric seawater electrolysis, and (D) cathode after asymmetric seawater electrolysis. Significant change to the electrode morphology is seen in (A) is attributed to the corrosion of the stainless steel after six hours of electrolysis. Catalyst loss is observed in (D) after 110 hours of asymmetric electrolysis.
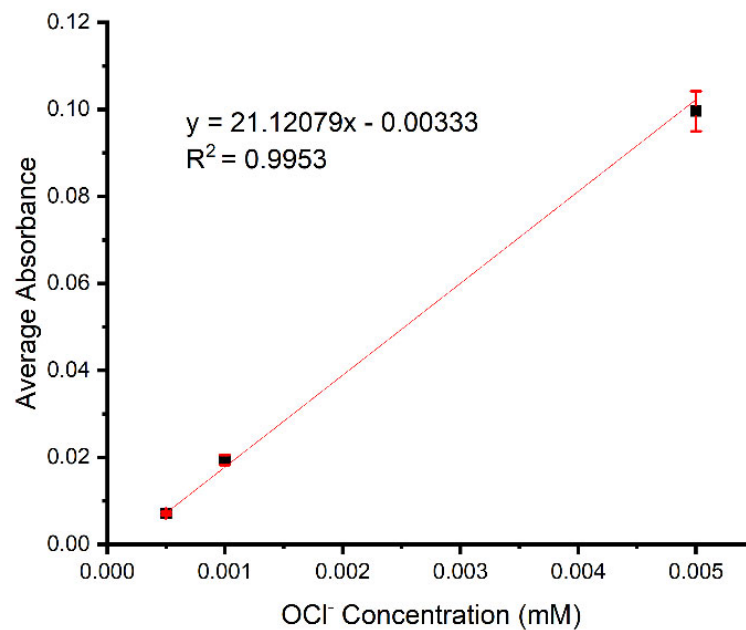
Figure S23. Free chlorine concentration calibration curve. Linear region of the free chlorine calibration curve obtained using DPD colorimetric UV-Vis analysis. Error bars (red bars) represent a single standard deviation from no less than three replicate measurements on three individually prepared samples.

Table S1. Average voltage degradation rates and standard deviations extracted from 6 h CP electrolysis of 0.5 M NaCl

	Avg_{50} (mV/h)	Avg_{100} (mV/h)	Avg_{250} (mV/h)	Avg_{500} (mV/h)
BPMWE	7.96	13.58	27.62	47.61
PEMWE	17.52	27.95	34.44	25.50
	Std_{50} (mV/h)	Std_{100} (mV/h)	Std_{250} (mV/h)	Std_{500} (mV/h)
BPMWE	15.13	12.02	7.73	24.58
PEMWE	12.00	8.04	21.33	13.55

Table S2. ICP-MS Analysis of dissolved metals (Fe, Ir, Pt) in the anode water feed after electrolysis

	Asymmetric			Symmetric	
	AEMWE (0.5 M NaCl)	BPMWE (Seawater)	PEMWE (Seawater)	BPMWE (Seawater)	PEMWE (Seawater)
Electrolysis time (h)	2.05	111	50.4	6.75	0.05
*$m_{dis,Fe}$ (µg)	31784	179.034	3.81	1810	N/A
$m_{dis,Ir}$ (µg)	3.3	3.744	N/A	N/A	0.13
$m_{dis,Pt}$ (µg)	0.49	0.218	0.71	0.7	0.27
*$r_{dis,Fe}$ (µg/hr)	15504	1.61	0.08	268.1	N/A
$r_{dis,Ir}$ (µg/hr)	1.6	0.03	N/A	N/A	2.63
$r_{dis,Pt}$ (µg/hr)	0.24	0.002	0.01	0.10	5.32

*We attribute trace Fe detected in the anolyte of PEMWE to minor corrosion of 316 SS electrolyzer input and output connections. Higher Fe signal detected in the BPMWE and AEMWE are attributed to corrosion of the 316 SS PTL substrate.

Table S3. ICP-MS analysis of Fe, Ir, Pt, in seawater and in the anode DI water feed prior to seawater electrolysis*

	Seawater	BPMWE (t = 0)	PEMWE (t = 0)
C_{Fe} (µg/L)	0.40	0.70	1.28
$C_{,Ir}$ (µg/L)	N/A	N/A	N/A
$C_{,Pt}$ (µg/L)	N/A	0.04	0.25

* The seawater column describes the concentration of Fe, Ir, and Pt in a representative sample of seawater. The BPMWE and PEMWE columns describe the concentration of Fe, Ir, Pt in DI water feeds after electrolyzer break-in procedure but prior to addition of seawater.

Supplemental Notes

Note S1. Chloride Oxidation Faradaic Efficiency Calculation

We calculated COR Faradaic efficiency using the equation below based on total free chlorine concentrations measured in the anode reservoir using colorimetric (UV-Vis) analysis:

$$FE\ (\%) = M \times V \times \frac{2\ mol\ e^-}{1\ mol\ COR\ Product} \times \frac{96485\ C}{1\ mol\ e^-} \times \frac{1}{Q} \times 100\%$$

Here, M is the total concentration in mol/L of free chlorine species (e.g. OCl^-, $HOCl$, Cl_2), V is the total volume (L) of solution, and Q is the total charge (coulombs) of charge passed in the experiment after NaCl was added to the cathode reservoir. We note that we assumed COR occurred only through the two-electron oxidation pathway (see section below), owing to the kinetic limitations expected for 4-, 6-, and 8-electron pathways to generate ClO_2^-, ClO_3^-, and ClO_4^-, respectively.

Note S2. Percent of Ionic Charge Carried by Cl^-

The "percent of ionic charge carried" by Cl^- is a metric describing the extent to which Cl^- was responsible for carrying ionic current between cathode and anode. This is with respect to other ions present which also may have contributed to the ionic current (e.g., H^+, OH^-, Na^+). For this calculation, we assumed that the only driving force for Na^+ crossover to the anode was diffusion as the electric field across the membrane would drive migration of positively charged species (Na^+) toward the cathode—thus all Na^+ ions that diffuse from cathode to anode must have been accompanied by Cl^-.

Under 'asymmetric' feed conditions, the $[Cl^-]$ in the anode reservoir represents both Cl^- that diffused to the anode in concert with Na^+ as well as Cl^- that was driven from cathode to anode and carried ionic current between the electrodes (**Figure 3c**, **middle panel**). We took the difference between $[Cl^-]$ and $[Na^+]$ in the anode reservoir to indicate the amount of Cl^- that carried ionic current over the course of the experiment, and used this value to calculate the percent of the total charge that carried between the electrodes that was supported by Cl^- using the following equation:

$$Charge\ Carried\ (\%) = (M_{Cl^-} - M_{Na^+}) \times V \times \frac{1\ mole\ e^-}{1\ mole\ Cl^-} \times \frac{96485\ C}{1\ mol\ e^-} \times \frac{1}{Q} \times 100\%$$

Here, V is the volume (L) of solution in the anode reservoir at t = 6 hr, and M_i is the concentration (mol L^{-1}) of species i in the anode reservoir at t = 6 hr.

Note S3. Strategies for Mitigating Chloride Oxidation

We considered two strategies for mitigating electrocatalytic chloride oxidation in membrane electrolyzers:

(A) Reducing $[Cl^-]$ at the membrane-anode interface. This should disfavor COR by both lowering the total reactant concentration in the reaction space as well as by thermodynamically disfavoring COR relative to OER (see **B**). While the composition of seawater is effectively fixed and as a result the bulk Cl^- cannot be modified without pre-treatment of electrolyzer input feeds, the local $[Cl^-]$ at the membrane-anode interface can be influenced using ion-selective membranes. For example, proton-exchange membranes (PEMs), can be used to inhibit anionic species from being transported to the anode interface.

(B) Using alkaline membrane/anode interfaces to thermodynamically disfavor the oxidation of Cl^- to free chlorine (i.e., Cl_2, $HOCl$, OCl^-) with respect to OER.[1] This should disfavor COR with respect to OER via the increased thermodynamic potential requirement for COR at high pH in comparison to low pH (see **Figure S12-S13**). Establishing alkaline membrane-electrode interface microenvironments should favor OCl^- as the

potential two-electron Cl^- oxidation product rather than $HOCl$ or Cl_2, affording maximal thermodynamic favorability for OER over COR. AEMs, with positive fixed charges in their polymer backbone, are intrinsically amenable to steady-state alkaline pH conditions. However, AEMs generally favor anion transport (e.g., Cl^-, see **Figure S2**) — this motivated our effort to synergistically leverage the ion-transport properties afforded by PEMs with the thermodynamically favorable microenvironment/alkaline conditions afforded by AEMs.

We also note that the identity of the two-electron Cl^- oxidation products are dictated by electrolyte pH, and as seen in the Pourbaix diagram (**Fig. S13**), the thermodynamic preference for OER over COR will increase at higher pH. We also note that other Cl^- oxidation products, including ClO_2^- ($4\ e^-$ oxidation), ClO_3^- ($6\ e^-$ oxidation), and ClO_4^- ($8\ e^-$ oxidation), have less positive standard potentials, but the increasingly complex nature of the $4\ e^-$, $6\ e^-$, $8\ e^-$ mechanisms required to generate these products suggest they will be kinetically difficult to produce.

Note S4. Electrochemical Impedance Analysis

We used electrochemical impedance spectroscopy (EIS) to provide a deeper understanding of the observed PEMWE and BPMWE cell voltage increases upon addition of NaCl. EIS has been previously demonstrated as a useful tool in evaluating water electrolysis performance, and we used it here to identify sources of performance limitation (e.g., series resistance, catalyst activity, etc.) as a function of current density and electrolyte composition.[2-4] For both BPMWE and PEMWE, galvanostatic electrochemical impedance spectroscopy (GEIS) was performed in a two-electrode configuration with the anode as the working and cathode as the counter electrode. GEIS was executed using a superimposed alternating current having an amplitude equal to 10% of the direct current density from a frequency of 300 kHz down to 20 mHz. **Figure S3** shows Nyquist plots and **Figure S4** shows tabulated results of 0 mA fixed current density GEIS scans for both architectures under several electrolyte configurations. To ascertain the effect of electrolyte presence and composition on membrane properties without the application of a constant current, we examined the high-frequency resistance for both electrolyzers as-assembled, with symmetric DI water fed conditions, with asymmetric 0.5 M NaCl fed conditions, and with symmetric 0.5 M NaCl fed conditions. **Figure S5** and **Figure S6** show Nyquist plots at each current density studied (50-500 mA cm^{-2}) for the PEMWE and BPMWE, respectively, both before adding 0.5 M NaCl to the cathode feed ("Before NaCl") and at several time points after adding NaCl to the cathode feed ("GEIS 10-16"). Guided by previously reported impedance studies, we observed that phenomena occurring at relatively high frequencies include both series resistance, and, in the case of the BPMWE, water dissociation impedance. These are taken to be the left-most x-axis intercept of both electrolyzer Nyquist plots and the left-most semicircle diameter of the BPMWE Nyquist plots, respectively.

In the absence of NaCl, the standard treatments of PEMWE behavior with a simplified Randles circuit (**Fig. S7A**) and BPMWE with a Randles circuit modified to account for the RC element associated with water dissociation impedance (**Fig. S7B**) yield interpretable and reasonable values of series resistance (R_s), charge-transfer resistance (R_{CT}), and water-dissociation resistance (R_{WD}).[2] However, upon addition of NaCl to the cathode feed of both electrolyzers, we observed significant inductive behavior at low frequencies (< 30 mHz) that is manifested as a positive imaginary component of the impedance (i.e. below the x-axis; note the sign of -Im(Z)). With the onset of this inductive behavior after adding NaCl, it is clear that the simplified circuits implemented in the DI H_2O case as shown in **Figure S7** are insufficient for extracting impedance information from low-frequency phenomena such as Faradaic charge transfer. We can see this in the PEMWE case shown in **Figure S8** where the DC point—that is, the low-frequency limit of the GEIS spectrum that should yield a resistance value that can be multiplied by the direct current density to yield the observed cell voltage under DC constant current conditions—does not agree with the total system resistance if the total resistance is taken to be the sum of R_s and R_{CT}, as was the case in the absence of NaCl. Discussions of the treatment of low-frequency induction in impedance spectroscopy exist in fuel cell and water electrolysis literature,[5-7] and the underlying cause of the observed behavior remains a challenging research question. Reliable treatment of this so-called "chemical inductance" phenomenon remains a question of interest in the field,[5] and robust analysis of the behavior observed in our system is a

target of our future work. In short, while high frequency regions of all Nyquist plots from NaCl experiments in **Figure S5-S6** are reliable for interpreting impedance, low frequency regions are not.

With this in mind, we assumed that the R_S and R_{WD} values extracted were from data at sufficiently high frequencies (> 1 kHz) as to be effectively independent of the observed "chemical inductance" that occurs below 30 mHz. Thus, **Figure S7** illustrates that neither R_s in the PEMWE or BPMWE, nor R_{WD} in the BPMWE, are sufficiently affected by the introduction of NaCl as to be the source of the significant voltage increases observed for both electrolyzer architectures. Hence, we attribute the spike in cell voltage to be predominantly sourced by some process or processes that strictly affect the Faradaic reactions at the cathode and/or the anode. This is in agreement with our proposed hypothesis regarding Na^+ exchange for H^+ in the Nafion reducing interface $[H^+]$.

Note S5. Stability Analysis

Figure S14 shows the V-t behavior of PEMWE and BPMWE electrolyzers over 6 hours with 0.5 M $NaCl_{aq}$ fed to the cathode and DI water fed to the anode. It appears that only at j = 500 mA cm^{-2} was electrolyzer durability improved for the PEMWE configuration over the BPMWE configuration, which may in part reflect BPM dehydration effects — H_2O transport to the water dissociation layer (WDL) may not have been sufficient to support necessary H^+ and OH^- fluxes that would maintain constant cathode and anode feed pH (**Figure S10B-C**).[8,9] Such a drop in WDL hydration could serve as the impetus for accelerated Cl^- transport toward the anode where corrosive free chlorine could be generated as a side product, although none was observed at these time scales.

While WDL dehydration may partially explain the increase in voltage degradation rate $\Delta V_{6\,h}$ as a function of applied current density for the BPMWE architecture, it has been observed that sufficiently positive potentials can facilitate the degradation of most carbon-based ionomeric polymers.[10–12] This degradation may be exacerbated by the presence of ionic species that can adsorb to the fixed charge groups of the ionomer. This adsorption would reduce membrane conductivity and subsequently lead to accelerated oxidative degradation of the membrane when cell voltages increase in response to the increased resistance. Still, it remains unclear what is the driving force for reducing the PEMWE degradation rate at 500 mA cm^{-2} relative to its degradation rate at lower current densities.

The correlation of PEMWE $\Delta V_{6\,h}$ with the free chlorine concentration after 6 hours of electrolysis (**Figure S17)** indicates a positive correlation with higher average concentrations of corrosive free chlorine species and higher rates of voltage degradation. While we expect that deleterious membrane oxidation will become operative to some extent at the PEM-anode interface of the PEMWE at all applied currents over the timescale of thousands of hours, the aforementioned scaling of performance loss in the presence of corrosive free chlorine suggests that the COR represents an additional failure mechanism for the PEMWE that is mitigated by the BPMWE.

In the case of the BPMWE, it is likely that the main drivers for performance loss over time are AEM oxidation/conductivity losses, as well as water transport limitations negatively impacting water dissociation kinetics within the BPM junction.

Following seawater electrolysis, post-mortem XPS analysis of electrode compositions (**Figure S18**) qualitatively revealed more IrO_x loss in the PEMWE anode over the course of longer electrolysis (asymmetric case, ~50 hours) which we attribute to OCl^- generation at the anode over time. In contrast, we observe a stronger IrO_x signal after shorter electrolysis (symmetric case, ~3 minutes), but also see a significant Mg signal which indicates that cathode precipitation was coupled with IrO_x dissolution to drive electrical disconnection and subsequently higher voltages in the PEMWE. As a comparison, **Figure S19** shows that in asymmetric seawater conditions, a significantly higher Ir signal remains on the BPMWE in comparison to symmetric seawater conditions. We attribute the signal in this former case to the lack of OCl^- generated at the anode, and in the latter case to a locally more acidic anode pH in the presence of seawater which appears to have driven stainless steel corrosion and subsequent IrO_x detachment.

Supplemental References

[S1.]   Dionigi, F., Reier, T., Pawolek, Z., Gliech, M., and Strasser, P. (2016). Design criteria, operating conditions, and nickel–iron hydroxide catalyst materials for selective seawater electrolysis. ChemSusChem *9*, 962–972. 10.1002/cssc.201501581.

[S2.]   Chen, L., Xu, Q., Oener, S.Z., Fabrizio, K., and Boettcher, S.W. (2022). Design principles for water dissociation catalysts in high-performance bipolar membranes. Nat Commun *13*, 3846. 10.1038/s41467-022-31429-7.

[S3.]   Blommaert, M.A., Vermaas, D.A., Izelaar, B., in 't Veen, B., and Smith, W.A. (2019). Electrochemical impedance spectroscopy as a performance indicator of water dissociation in bipolar membranes. J. Mater. Chem. A *7*, 19060–19069. 10.1039/C9TA04592A.

[S4.]   Yang, G., Yu, S., Li, Y., Li, K., Ding, L., Xie, Z., Wang, W., Dohrmann, Y., and Zhang, F.-Y. (2021). A simple convertible electrolyzer in membraneless and membrane-based modes for understanding water splitting mechanism. Journal of Power Sources *487*, 229353. 10.1016/j.jpowsour.2020.229353.

[S5.]   Bisquert, J., and Guerrero, A. (2022). Chemical inductor. J. Am. Chem. Soc. *144*, 5996–6009. 10.1021/jacs.2c00777.

[S6.]   Pivac, I., and Barbir, F. (2016). Inductive phenomena at low frequencies in impedance spectra of proton exchange membrane fuel cells – A review. Journal of Power Sources *326*, 112–119. 10.1016/j.jpowsour.2016.06.119.

[S7.]   Shkirskiy, V., King, A.D., Gharbi, O., Volovitch, P., Scully, J.R., Ogle, K., and Birbilis, N. (2015). Revisiting the electrochemical impedance spectroscopy of magnesium with online inductively coupled plasma atomic emission spectroscopy. ChemPhysChem *16*, 536–539. 10.1002/cphc.201402666.

[S8.]   Bui, J.C., Digdaya, I., Xiang, C., Bell, A.T., and Weber, A.Z. (2020). Understanding multi-ion transport mechanisms in bipolar membranes. ACS Appl. Mater. Interfaces *12*, 52509–52526. 10.1021/acsami.0c12686.

[S9.]   Oener, S.Z., Twight, L.P., Lindquist, G.A., and Boettcher, S.W. (2021). Thin cation-exchange layers enable high-current-density bipolar membrane electrolyzers via improved water transport. ACS Energy Lett. *6*, 1–8. 10.1021/acsenergylett.0c02078.

[S10.]   Lindquist, G.A., Xu, Q., Oener, S.Z., and Boettcher, S.W. (2020). Membrane electrolyzers for impure-water splitting. Joule *4*, 2549–2561. 10.1016/j.joule.2020.09.020.

[S11.]   Li, D., Matanovic, I., Lee, A.S., Park, E.J., Fujimoto, C., Chung, H.T., and Kim, Y.S. (2019). Phenyl oxidation impacts the durability of alkaline membrane water electrolyzer. ACS Appl. Mater. Interfaces *11*, 9696–9701. 10.1021/acsami.9b00711.

[S12.]   Ayers, K., Danilovic, N., Ouimet, R., Carmo, M., Pivovar, B., and Bornstein, M. (2019). Perspectives on low-temperature electrolysis and potential for renewable hydrogen at scale. Annu. Rev. Chem. Biomol. Eng. *10*, 219–239. 10.1146/annurev-chembioeng-060718-030241.